XIST Self-regulates its Association with THOC2 and the Nuclear Epigenetic Machinery via miR-186 in Alzheimer's disease

Somenath Sen and Debashis Mukhopadhyay*

Biophysical Sciences Group, Saha Institute of Nuclear Physics, A CI of Homi Bhabha National Institute, Kolkata 700 064, India.

* To whom correspondence should be addressed. Email: debashis.mukhopadhyay@saha.ac.in, Tel: +91-33-2337 5345

Running Title: Cytoplasmic XIST Regulates Its Nuclear Interactions via miR-186.

Graphical Abstract

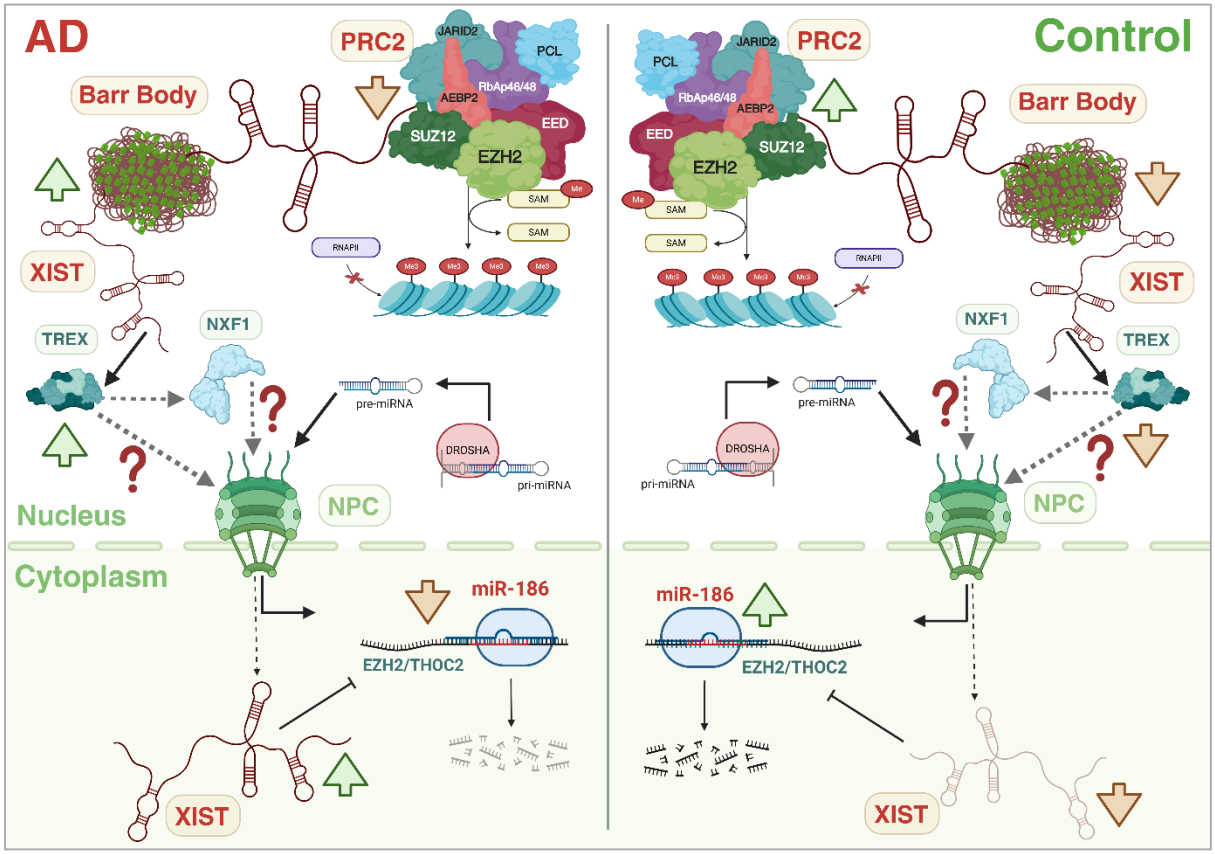

Abstract

Alzheimer's disease (AD) exhibits a strong female bias, yet the underlying molecular basis remains poorly understood. This study identifies the long non-coding RNA (lncRNA) XIST, a master regulator of X-chromosome inactivation (XCI), as a driver of female-specific AD pathology. Single-nucleus RNA-seq (snRNA-seq) analyses from human AD cortex and *in vitro* AD models reveal elevated and abnormally cytoplasmic XIST, a feature not previously reported in neurodegeneration. Reduced EZH2 levels in AD impair histone H3 lysine-27 trimethylation (H3K27me3) on the inactive X chromosome, disturbing epigenetic silencing. The epigenetic dysregulation elevates the X-linked RNA export factor THOC2, which participates in a feedback loop with XIST. Cytoplasmic XIST functions as a competing endogenous RNA (ceRNA) by sequestering miR-186-5p, thereby rescuing EZH2 and THOC2 transcripts. The resulting XIST/miR-186/EZH2/THOC2 axis couples XIST-driven epigenetic changes with nuclear RNA export pathways via cytoplasmic XIST. Disrupted EZH2-XIST interaction reduces H3K27me3 marks on the inactive X, while increased THOC2 promotes THOC2(TREX)-XIST interaction, maintaining the harmful feedback. Our findings reveal a novel mechanism through which XIST gets recruited to the nuclear RNA export pathways in AD. XIST thus emerges as a critical node in sex-specific AD pathophysiology and a promising target for therapeutic intervention.

Keywords: Alzheimer's disease, XIST, lncRNA, X-chromosome inactivation, miR-186, EZH2, THOC2, ceRNA.

Introduction

Alzheimer's disease (AD) is an increasing global health challenge, mainly affecting the elderly and characterized by progressive cognitive decline and memory loss. The disease develops as amyloid β (Aβ) plaques and neurofibrillary tangles (NFTs) accumulate in the brain, leading to neuronal dysfunction and ultimately cell death [1]. Despite extensive research, the exact molecular mechanisms behind AD development are not fully understood, highlighting the need for further investigation into the disease's underlying regulation.

Recent advances have highlighted the importance of long non-coding RNA (lncRNAs) in influencing various factors behind AD, including gender [2]. Two-thirds of all AD cases are attributed to females [3], and this discrepancy remains unexplained. Recent research has identified sex-specific lncRNA candidates that are dysregulated in AD [4], [5]. One such lncRNA is X-inactive specific transcript (XIST), which plays the major role in X-chromosome dosage compensation [6], is notably upregulated in AD [7]. X-chromosome inactivation is a unique process for maintaining equal expression levels of sex-linked genes, despite females having an extra X chromosome [8]. Consequently, females naturally exhibit higher levels of XIST [9]. Here, we investigate the potential role of XIST as a regulator of the female bias in AD.

XIST is traditionally known to mediate X-inactivation by interacting with the PRC2 complex. A component of this complex, EZH2, functions as a catalytic subunit and promotes the methylation of histone H3 at lysine 27 (H3K27me3) [10]. This histone modification leads to transcriptional repression of the inactivated X chromosome [11]. However, there are more complex roles of XIST beyond X-chromosome inactivation (XCI), especially in the context of various diseases [12], [13], [14]. In proliferative scenarios like many cancer types, XIST acts as an oncogene through its interactions [15], [16], making its upregulation in neurodegeneration particularly unprecedented.

Additionally, challenging the traditional view of XIST's nuclear localization and retention, a recent study has shown its presence in the cytoplasm under proinflammatory stress [17]. While the cytoplasmic presence of XIST has already been noted in AD [7], the mechanistic details remain unclear. XIST is upregulated and acts as a sponge for miR-186-5p in non-small cell lung cancer, influencing invasion and proliferation [18]. We explored the potential role of the miR-186/XIST axis in AD. Interestingly, in the aging brain, miR-186 is significantly decreased and negatively regulates BACE1 expression, a key gene involved in Aβ production in AD [19]. Although how XIST is present in the cytoplasm is not fully understood, some mRNA export

103 factors are known to facilitate nuclear export of lncRNAs [20]. While reduced NXF1/XIST
104 interaction promotes XIST's accumulation in the nucleus [21], we hypothesize that the TREX
105 complex may help overcome this obstacle. The *THOC2* gene encodes the largest subunit of the
106 TREX complex which has been reported to interact with both mRNA and lncRNA, aiding their
107 export [20], [22]. Notably, the *THOC2* gene itself is X-linked [22]. This prompted us to
108 investigate the regulatory loop bridging XIST's role in the functioning of the nuclear RNA
109 export machinery.
110 Here, we demonstrate that the abnormal presence of XIST in the cytoplasm contributes to its
111 overall upregulation in AD and further examine its functional impact on nuclear and
112 cytoplasmic processes. Using an *in vitro* AD model, we show that by sponging miR-186,
113 cytoplasmic XIST preserves EZH2 levels, and reduces THOC2 mRNA degradation, leading to
114 increased THOC2-XIST physical association, which links XIST to the RNA export pathways,
115 hinting towards its own nuclear export. These novel findings shed light on the sex bias observed
116 in AD.

117 **Materials and Methods**

118 **Single-nucleus RNA-seq (snRNA-seq) Data Analysis of AD**

119 ***Data Acquisition and Preprocessing***

120 To perform snRNA-seq data analysis of human AD brain samples, the raw Count Matrix and
121 metadata files were obtained from the Gene Expression Omnibus database (GEO) [23] for the
122 GSE138852 dataset. The dataset included information from 8 10X libraries (4 AD and 4
123 Control), with each library comprising two individuals, totaling n = 16. The Seurat package in
124 R (v4) (https://satijalab.org/seurat/) was used to run the snRNA-seq pipeline. In total, we
125 analyzed 6673 nuclei from AD samples and 6541 nuclei from control samples. In case of
126 female tissues, 2605 nuclei from AD samples and 1122 nuclei from control samples were
127 analyzed.

128 ***Sex-specific subsetting***

129 To perform sex-specific snRNA-seq analysis, the Seurat object created with the Seurat package
130 in R was split into male and female subsets. The sex information was separately added to the
131 metadata, which was then integrated to subset the Seurat object.

132 ***Quality Control, Filtering, and Normalization***

133 Low-quality nuclei were removed from downstream analysis by applying the following
134 filtering parameters. We excluded nuclei with less than 50 features or more than 5000 features.
135 The ribosomal content tolerance threshold was set at 10% to remove doublets or degraded
136 nuclei. Next, the Seurat object was normalized using log normalization, and the 2000 most
137 variable features were selected using the vst feature selection method.

138 ***Dimensionality Reduction and Clustering***

139 Data were scaled and centered, followed by Principal Component Analysis (PCA). The optimal
140 number of principal components (PCs) was determined using an ElbowPlot, and the first 10
141 PCs were selected for clustering. Nuclei were clustered using the Louvain algorithm [24].
142 Uniform Manifold Approximation and Projection (UMAP) was applied for visualization.

143 ***Cell Type Annotation and Subclustering***

144 For each nucleus, neuronal cell types were identified using nuclear-enriched neuronal markers
145 NeuN, ELAVL3, and SYT1, as well as from the metadata. The neuronal nuclei subset was then
146 extracted for further analysis to find differentially expressed genes between AD and Control.

147 ***Differential Expression Analysis***

148 The differential expression analysis was conducted using the Wilcox rank-sum test [25], and
149 an adjusted p-value of <0.05 was used as the cutoff to identify significant dysregulation. The
150 expression data from AD and control samples were extracted from the output and plotted using
151 GraphPad Prism 9 (https://www.graphpad.com/).

152 ***Functional Enrichment Analysis***

153 Using Pearson's correlation analysis, the transcriptional changes positively and negatively
154 correlated with XIST expression were calculated. The top 50 correlated genes were visualized
155 using the Pheatmap package in R. Based on these co-expressed genes, the pathways mediated
156 by XIST were enriched through Gene Set Enrichment Analysis (GSEA) with the clusterProfiler
157 package (version 4.14.6) [26] in R. The enriched pathways were then categorized into inhibited
158 and promoted pathways based on their negative (<0) and positive (>0) Normalized Enrichment
159 Score (NES) values, respectively. The top 10 inhibited and promoted pathways were displayed
160 in a dotplot using the ggplot2 package in R [27].

161 **Cell Culture and Plasmid Transfection**

The human neuroblastoma cell line SH-SY5Y was obtained from the National Centre for Cell Sciences (NCCS, Pune, India), cell repository. The cells were cultured in Dulbecco's Modified Eagle Medium/Nutrient Mixture F-12 (DMEM-F12, Gibco) supplemented with 10% fetal bovine serum (FBS, Gibco), following standard protocols provided by the supplier. Cell maintenance was performed under controlled conditions in a humidified incubator (Thermo Scientific) set at 37°C with 5% CO2 atmosphere to ensure optimal growth conditions.

For transfection experiments, cells at 70-80% confluency were chosen to ensure optimal transfection efficiency. Lipofectamine 2000 transfection reagent (Invitrogen) was used for all transfection procedures, with the reagent volume set to twice the amount (in microliters) of the plasmid DNA (in micrograms) as recommended by the manufacturer's protocol. To evaluate transfection efficiency, green fluorescent protein (GFP)-tagged constructs were introduced, and cellular fluorescence was examined after a 48-hour incubation period using fluorescence microscopy. This quality control step verified successful transfection before moving on to subsequent experiments. All procedures were performed under sterile conditions in a laminar flow hood to maintain cell culture integrity.

Plasmid Constructs, siRNAs and Antibodies

Plasmids

The GFP control plasmid (pGFP-C1, Clontech) and the amyloid precursor protein intracellular domain (AICD) construct cloned into the pGFP-C1 vector (referred to as AICD from here on) were available in the laboratory. These constructs had been previously created and characterized in earlier studies [28], [29], [30], [31]. The GFP plasmid served as the baseline control vector, while the AICD construct contained the APP intracellular domain sequence inserted into the same pGFP-C1 backbone. All the constructs were stored as glycerol stocks at liquid nitrogen. Before transfection, plasmid isolation was performed using the Miniprep plasmid kit (Qiagen, Cat No. # 27104). The integrity of all constructs was confirmed by running the purified plasmids on 0.8% agarose gels.

siRNAs

XIST was knocked down using pre-designed siRNAs (Qiagen, Cat No. #1027415). The transfection was performed at a final concentration of 50 nM. All the transfections were performed using Lipofectamine 2000 (Invitrogen) at 37°C.

Antibodies

193 THOC2 Polyclonal Antibody (Invitrogen, Cat No. #PA5-110485), Ezh2 (AC22) Mouse mAb
194 (Cell Signaling Technology, Cat No. #3147S), Anti-Histone H3 (tri methyl K27) antibody
195 (Abcam, Cat No. #ab192985), Normal Rabbit IgG (Cell Signaling Technology, Cat No. #2729),
196 Normal Mouse IgG (Cell Signaling Technology, Cat No. #68860).

197 **AD Cell Model**

198 The SH-SY5Y human female neuroblastoma cells were transfected with either the GFP control
199 vector or AICD construct using Lipofectamine 2000 transfection reagent according to standard
200 protocols. Synthetic amyloid-β peptide ($A\beta_{1-42}$, Sigma) was prepared by dissolving the
201 lyophilized powder in dimethyl sulfoxide (DMSO) to make a stock solution.
202 Three hours after transfection, specific treatments were applied: GFP-transfected cells received
203 DMSO, while AICD-expressing cells were treated with 0.5 μM $A\beta_{1-42}$ solution. After a 48-hour
204 incubation under standard culture conditions, all samples were harvested for further
205 experiments. The GFP-transfected, DMSO-treated cells served as the control group, while the
206 AICD-expressing, $A\beta_{1-42}$-treated cells represented the AD cell model, as previously
207 characterized (Supplementary Figure S1) [5], [32], [33]. All experimental conditions were
208 conducted simultaneously with the exact passage numbers and culture conditions to reduce
209 variability.

210 **RNA Isolation, cDNA Conversion, and Quantitative Real-time PCR**

211 Total RNA was extracted from the harvested cells using TRIzol reagent (Invitrogen, USA)
212 following the manufacturer's recommended protocol. RNA concentration and purity were
213 measured with a Nanodrop 2000 spectrophotometer (Thermo Scientific), and samples were
214 accepted for further processing only if they showed absorbance ratios ~ 2.0 at 260/280 and
215 260/230, indicating minimal protein or organic compound contamination.
216 For cDNA synthesis, 2 μg of purified total RNA was reverse transcribed for each experimental
217 condition. The reverse transcription process was optimized for different RNA species. The
218 oligo(dT)18 primers (Thermo Scientific) were used for mRNA conversion, random hexamers
219 (Thermo Scientific) were employed for lncRNA templates, and stem-loop primers (Eurofins)
220 were used for miRNA reverse transcription following the pulse PCR methodology [34]. The
221 reactions were conducted using a standardized master mix containing 5× reaction buffer, 10
222 mM dNTP mix, primers, and reverse transcriptase enzyme (Thermo Scientific).
223 Quantitative real-time PCR was carried out on a QuantStudio™ 3 Real-Time PCR System
224 (Applied Biosystems) using 2X SYBR™ Green PCR Master Mix (Applied Biosystems) and

225 gene-specific primers (Supplementary Table S1). Appropriate endogenous controls were
226 chosen based on transcript type. The 18S rRNA served as the reference for non-coding RNAs,
227 while β-Actin was used for protein-coding gene normalization. Relative gene expression levels
228 were calculated using the $2^{-\Delta\Delta Ct}$ method, with all reactions performed in technical replicates to
229 ensure consistency. Thermal cycling conditions adhered to manufacturer guidelines, including
230 an initial denaturation at 95°C for 10 minutes, followed by 40 cycles of 95°C for 15 seconds
231 and 60°C for 1 minute, ending with a melt curve analysis to confirm amplification specificity.

232 **Western Blot**

233 Cells were grown in 6-well plates (Tarsons) and washed twice with 1X PBS before being
234 harvested. The cells were then scraped using a cell scraper and lysed with cell lysis buffer (1M
235 Tris-HCl (pH 7.5), 1N NaCl, 0.5M EDTA, 1M NaF, 1M Na3VO4, 10% SDS, 20mM PMSF,
236 10% Triton X-100, and 50% glycerol, 1X protease inhibitor) , and kept on ice for 30 minutes.
237 After incubation, the lysate was spun at 13,000 RPM at 4°C. The pellet was discarded, and the
238 supernatant was used to measure protein concentration using the Bradford assay. The lysates
239 were then loaded onto an 8% SDS-PAGE gel with gel loading dye containing bromophenol
240 blue. Proteins were transferred from the gel to a PVDF membrane (Millipore, Billerica, MA,
241 USA). The membrane was blocked with 5% non-fat dried milk dissolved in TBST (50 mM
242 Tris-HCl, 150 mM NaCl pH 7.5, with 0.05% Tween 20) for one hour, followed by washing
243 with TBST. It was then incubated overnight at 4°C with primary antibody diluted 1:1000 in
244 TBST with shaking. After overnight incubation, the membrane was washed thrice with TBST
245 and then incubated with secondary antibody in TBST (1:3000) for two hours at room
246 temperature. Following secondary antibody incubation, the membrane was washed thrice with
247 TBST. Bands were visualized using the Super Signal West Pico Chemiluminescent Substrate
248 kit (Thermo Scientific, IL, USA) on an Azure Biosystems Imager.

249 **Combined Immunocytochemistry & Fluorescence in situ Hybridization of RNA (ICC-**
250 **FISH)**

251 The ICC-RNA-FISH experiments were conducted following the protocol for adherent cell lines
252 as outlined by Stellaris with modifications. Cells were seeded on a 22 mm coverslip placed in
253 a 35 mm cell culture dish two days before transfections. After transfections and treatments, the
254 cells were first washed twice with autoclaved 1X PBS. The cells were then fixed using 4%
255 paraformaldehyde (Merck) (PFA) for 10 minutes at room temperature. Subsequently, the 4%
256 PFA was discarded, followed by two washes with 1X PBS. Cells were permeabilized with 0.5%

257 Triton X (Promega) for 5 minutes, then washed twice with 1X PBS. This permeabilization step
258 was repeated once more. After the final wash with 1X PBS, the cells were immersed in 500 µl
259 of primary antibody diluted in 1X PBS (1:500). Cells were incubated with the primary antibody
260 for 2 hours, then washed twice with 1X PBS for 5 minutes each. Next, the cells were incubated
261 with secondary antibody diluted in 1X PBS (1:1000) for 2 hours. The secondary antibody
262 solution was discarded, and the cells were washed twice with 1X PBS for 5 minutes each. After
263 the second wash, the cells were immersed in 4% PFA for 10 minutes to stabilize protein-protein
264 interactions. Following this, the cells were washed twice more with 1X PBS.
265 Next, the cells were submerged in 500 µl of wash buffer A (Stellaris) for 5 minutes. The
266 coverslips were moved to a humidified chamber and placed on top of 100 µl of hybridization
267 solution containing RNA FISH probes diluted in the hybridization buffer (Stellaris) at 1:250.
268 They were then incubated overnight at 37°C. After the overnight incubation, the cells were
269 washed with wash buffer A (Stellaris) for 30 minutes. The coverslips were then mounted on
270 glass slides using 1X PBS containing DAPI (1 µg/µl) as the mounting medium. The coverslips
271 were left to incubate at room temperature for 30 minutes and sealed to prevent drying. The
272 slides were stored at 4°C.

273 **3D Colocalization Analysis from Confocal and Super-resolution Imaging Data**

274 ICC-FISH slides were imaged using confocal and super-resolution settings on a Zeiss LSM
275 880 with Airyscan 2 microscope across multiple z-planes. The raw data from the microscope
276 were analyzed using the Fiji software [35]. First, the ROIs were selected for each colocalizing
277 channel. The selected ROIs were then extracted individually containing the z hyperstacks for
278 each channel. Next, the 3D ROIs were analyzed using the Coloc 2 (https://imagej.net/plugins
279 /coloc-2) plugin in Fiji to calculate the Pearson's colocalization coefficient (r value). The Z-
280 stack Depth Color Code (https://github.com/UU-cellbiology/ZstackDepthColorCode) plugin
281 was used to determine the depth of each stack for each colocalizing channel.

282 **Nuclear and Cytoplasmic RNA Extraction**

283 RNA isolation from the nuclear and cytoplasmic fractions of the cells was performed using the
284 RNA Subcellular Isolation Kit (Active Motif) following the manufacturer's instructions with
285 modifications. All the centrifugation steps were carried out at 4°C in a refrigerated centrifuge
286 (Thermo). Cells were washed twice with pre-chilled 1X PBS and collected using a cell scraper
287 (Tarsons). The detached cells were collected in microcentrifuge tubes and spun at 2,500 RCF
288 for 5 minutes. The supernatant was discarded, followed by a final wash in pre-chilled 1X PBS.

289 The cells in the pellets were then lysed with ice-cold lysis buffer and kept on ice for 20 minutes,
290 mixed by vortexing and inversion every 3 minutes. Proper rupture of the cell membrane and
291 the presence of free nuclei were monitored under an inverted phase-contrast microscope
292 (Zeiss). After incubation, the tubes were spun at 14,000 RPM for 5 minutes to pellet the nuclei.
293 The supernatants containing the cytoplasmic fractions were transferred to a new tube. The
294 nuclear pellet was washed with 200 µl of 70% ethanol at 14,000 RPM for 5 minutes. Next, 250
295 µl and 350 µl of buffer G containing β-mercaptoethanol (Sigma) for cytoplasmic and nuclear
296 fractions, respectively, were added to their respective tubes. The tubes were vortexed at
297 maximum speed for 30 seconds, then 350 µl of pre-chilled molecular grade 70% ethanol
298 (Sigma) was added to each tube. The solution was homogenized by pipetting up and down
299 using a P200 pipette tip. The nuclear and cytoplasmic lysates were then transferred to their
300 respective purification columns and washed with 650 µl of wash buffer. Following a final wash
301 with pre-chilled 70% ethanol (Sigma), the columns were spun at 14,000 RPM for another 1
302 minute to remove any residual ethanol. RNA was eluted by adding nuclease-free water
303 (Promega) directly into the columns and spinning at 14,000 RPM for 2 minutes.

304 **RNA Immunoprecipitation (RIP)**

305 The RIP experiments were carried out following the abcam's RIP protocol
306 (https://www.abcam.com/protocols/RIP) with some modifications. Cells were harvested by
307 trypsinization and then resuspended in ice-cold PBS, freshly prepared nuclear isolation buffer
308 (1.28 M sucrose, 40 mM Tris-HCl, pH 7.5, 20 mM $MgCl_2$, 4% Triton X-100), and nuclease
309 water. The suspension was incubated on ice for 20 minutes with intermittent mixing and
310 vortexing to ensure thorough lysis. The nuclei were then pelleted by centrifugation at 2,500 ×
311 g for 15 minutes. The resulting pellet was resuspended in freshly prepared RIP buffer (150 mM
312 KCl, 25 mM Tris, pH 7.4, 5 mM EDTA, 0.5 mM DTT, 0.5% NP-40, 100 U/ml RNase inhibitor,
313 and protease inhibitors) and kept on ice for 20 minutes with frequent mixing and vortexing.
314 Sonication of the nuclear fraction was performed using the following settings: 30% amplitude
315 for 20 seconds with 30-second intervals, repeated three times. The mixture was then nutated at
316 20 rpm for 90 minutes at 4°C. After nutation, centrifugation was performed at 12,000 × g for
317 20 minutes at 4°C to obtain the nuclear lysate. The pellet was discarded, and the supernatant
318 was used for protein quantification via the Bradford assay. For each sample, 5 mg of total
319 protein in RIP buffer was combined with 2.5 µg of target antibody or IgG and incubated
320 overnight at 4°C with gentle rotation. Protein A/G magnetic beads (25 µl) (Thermo) were added
321 to each reaction and incubated for 2 hours at 4°C with gentle rotation. Beads were separated

322 on a magnetic rack; the supernatant was discarded. The beads were washed by resuspending
323 them in 500 µl of RIP buffer, with four washes performed in total. Co-precipitated RNAs were
324 extracted by resuspending the beads in 500 µl of TRIzol reagent, following the manufacturer's
325 protocol.

326 **Chromatin Immunoprecipitation (ChIP)**

327 ChIP was performed using the SimpleChIP ® Enzymatic Chromatin IP Kit (Cell Signaling
328 Technology, Cat No. #9003) following the manufacturer' s instructions with modifications.
329 Briefly, cells were crosslinked by adding formaldehyde to a final concentration of 1% and
330 incubated at room temperature for 10 minutes with gentle rocking. Crosslinking was then
331 quenched with 1.25 M glycine (final concentration 0.125 M) for 5 minutes at room temperature.
332 Cells were washed twice with ice- cold 1 X PBS and collected by centrifugation. Cell pellets
333 were lysed with cell lysis buffer supplemented with protease inhibitors and DTT, then
334 incubated on ice for 15 minutes with frequent vortexing to promote lysis. Nuclei were pelleted
335 at 2,500 g for 5 minutes. The nuclear pellet was washed with 1X wash buffer containing DTT.
336 The nuclei were digested with micrococcal nuclease (Takara) at 37 ° C for 20 minutes. After
337 digestion, the pellet was resuspended in 1X ChIP buffer with protease inhibitors. The nuclear
338 pellet was lysed on ice for 15 minutes with frequent vortexing, followed by sonication to shear
339 chromatin to approximately 150-900 bp. Fragmentation was confirmed via agarose gel
340 electrophoresis. The nuclear debris were pelleted at 9,500 g for 10 minutes, and the supernatant
341 was transferred to a new tube. A Bradford assay was used to measure protein concentrations.
342 Equal amounts of chromatin were diluted in 1X ChIP buffer and incubated overnight at 4°C
343 with 2 µg of antibody against H3K27me 3 (Abcam, # ab 192985). Normal rabbit IgG (Cell
344 Signaling Technology) was used in parallel as a negative control. 2% of input chromatin lysate
345 was reserved. Antibody–chromatin complexes were pulled down with protein G magnetic
346 beads by rotating at 4 ° C for 2 hours. Beads were washed sequentially with low-salt and high-
347 salt buffers to remove nonspecific interactions. Bound chromatin and the 2% input samples
348 were eluted in elution buffer using a thermomixer (Labman) for 30 minutes at 1200 RPM at
349 65°C. The eluted chromatin was digested with proteinase K at 65°C for 2 hours at 1200 RPM
350 to degrade proteins. DNA was purified with spin columns from the kit and eluted in 15 µL of
351 nuclease- free water. Immunoprecipitated DNA was analyzed by quantitative PCR (qPCR) with
352 locus-specific primers and normalized using the 2% input samples.

353 **Biotinylated miR-186-5p Mimic Overexpression and RNA Pull-down**

354 The 3' biotinylated miRNA mimic of miR-186-5p was purchased from Qiagen. The mimic was
355 transfected at a final concentration of 60 nM using Lipofectamine 2000 (Invitrogen)
356 transfection reagent according to the manufacturer's protocol. Cells were harvested 48 hours
357 after transfection. The RNA pull-down was performed following the pre-established protocol
358 [36]. Cells were washed twice with ice-cold 1× PBS and then harvested by trypsinization and
359 scraping, followed by centrifugation at 2,000 × g for 5 minutes at 4 °C. The resulting cell pellets
360 were transferred to pre-chilled microcentrifuge tubes and either processed immediately or
361 stored at −80 °C. 550 µl of freshly prepared lysis buffer (20 mM Tris-HCl pH 7.5, 100 mM
362 KCl, 5 mM $MgCl_2$, 0.3% NP-40) supplemented with protease and RNase inhibitors was added
363 to each pellet. Cells were lysed by pipetting up and down and incubated on ice for 20 minutes
364 with frequent intermittent mixing to promote lysis. Lysates were spun by centrifugation at
365 18,000 × g for 10 minutes at 4 °C, and supernatants containing the cytoplasm were collected
366 for subsequent analysis. In parallel, 50 µl of Dynabeads™ MyOne™ Streptavidin T1 beads
367 (Invitrogen) per sample were prepared by sequential washes: twice with Solution A (0.1 M
368 NaOH, 0.05 M NaCl), twice with Solution B (0.1 M NaCl, 70% ethanol), and three times with
369 lysis buffer. Beads were then blocked in 500 µl lysis buffer containing BSA (Merck) and yeast
370 tRNA (Invitrogen) by rotating at 4 °C for 2 hours. After blocking, beads were briefly washed
371 with lysis buffer and incubated with 500 µl of cytoplasmic lysate overnight at 4 °C with gentle
372 rotation. The remaining 50 µl aliquot of each lysate was retained and stored at −80 °C for 10%
373 input RNA extraction. The next day, beads were washed four times with 500 µl of lysis buffer
374 to remove non-specific interactions. For RNA extraction, both the pull-down samples and
375 stored input lysates were mixed with 500 µl TRIzol, then stored at −20 °C till the RNA isolation
376 initiation step.

377 **Statistical Analysis**

378 Statistical analyses were conducted to assess the significance of the experimental results. For
379 comparisons between two groups, an unpaired student's t-test and in case of more than two
380 groups one-way ANOVA followed by Bonferroni post hoc test was performed using GraphPad
381 Prism (version 9), available at (https://www.graphpad.com/). The p-values from snRNA-seq
382 data analyses were generated by the Seurat package (v4) (https://satijalab.org/seurat/). All
383 statistical tests were carried out with at least three independent biological replicates to ensure
384 the reliability of the results.
385 The threshold for statistical significance was set as follows: results with p-values of 0.05 or
386 higher were considered statistically non-significant and labeled as "ns" (not significant).

Results with p-values less than 0.05 were marked with a single asterisk (*), indicating significance at the 95% confidence level. P-values below 0.01 were denoted by double asterisks (**), those under 0.001 were shown with triple asterisks (***), and those under 0.0001 were shown with triple asterisks (****). This notation system was applied consistently across all figures and tables to clearly indicate the statistical significance of all reported results.

Results

XIST upregulation in the AD brain results in synaptic transmission and transcriptional repression

The snRNA-seq analysis pipeline was used to examine XIST expression across different cell types in female AD and control brain samples from the GSE138852 dataset. Neuronal nuclei were confirmed through enrichment of canonical neuronal markers and the dataset metadata. Visualization on the UMAP plot showed colocalization of XIST with ELAVL3, demonstrating strong XIST expression in neuron-derived nuclei (Figure 1.A.1.). Notably, female neuronal cells in AD showed a marked upregulation of XIST, a trend also observed when averaging across all the annotated cell types in the tissue (Figure 1.A.2., A.3.).

To evaluate the biological implications of XIST upregulation in AD, Pearson's correlation analysis was conducted, revealing genes that are co-expressed with increased XIST levels in female neurons (Supplementary Figure S2.).

Subsequent Gene Set Enrichment Analysis (GSEA) of the co-expressed genes revealed biological pathways linked to changes in XIST expression. Pathways with significant negative enrichment scores included cytoplasmic translation (GO:0002181), synaptic vesicle fusion with the presynaptic active zone membrane (GO:0031629), and synaptic vesicle membrane organization (GO:0048499), indicating a decrease in synaptic and translational activities. Conversely, pathways associated with high XIST expression that showed positive enrichment scores included, sex-chromosome dosage compensation (GO:0007549), and post-transcriptional gene silencing (GO:0016441), suggesting increased heterochromatinization and RNA-mediated silencing (Figure 1.B., Supplementary Table S2.).

Taken together, these analyses suggest that XIST upregulation in AD neurons may contribute to impaired synaptic function and decreased protein synthesis, while also promoting transcriptional repression and epigenetic remodeling. This positions XIST as a potential regulator of neuronal dysfunction in AD.

XIST is aberrantly upregulated in the cytoplasm in AD

419 The functional enrichment analysis identified XIST as a key regulator in promoting
420 neurodegeneration in AD. To gain a better understanding of its role, XIST expression and its
421 subcellular localization were examined in an *in vitro* AD model (Figure 2.A.) using
422 fractionation-qPCR and RNA-FISH.
423 Using RNA-FISH followed by confocal imaging, it was observed that the most intense XIST
424 signals were concentrated on the inactivated X chromosome, appearing as a distinct bright red
425 punctum in the nucleus that co-localized with DAPI. Interestingly, a notable presence of XIST
426 in the cytoplasm was also detected (Figure 2.B.); an atypical and previously uncharacterized
427 localization in the context of AD. This unusual cytoplasmic presence suggests a potentially
428 novel function of XIST in the disease pathology.
429 The qPCR analysis confirmed that total XIST expression was significantly upregulated in the
430 AD model (Figure 2.C.). To further clarify this upregulation, subcellular fractionation-qPCR
431 combined with RNA-FISH-based intensity measurements were used to separately quantify
432 nuclear and cytoplasmic XIST levels. In both control and AD cells, nuclear XIST levels were
433 substantially higher than cytoplasmic levels. However, when comparing nuclear and
434 cytoplasmic XIST levels between AD and control conditions, it was observed that, along with
435 the significant increase in nuclear XIST in AD, cytoplasmic XIST levels were also markedly
436 elevated compared to controls. Interestingly, the upregulation in the cytoplasmic XIST was
437 more drastic compared to the nuclear transcript pool (Figure 2.C.1.-C.4.). The SCARNA9 RNA
438 expression was mainly localized to the nucleus, while tRNA expression was predominantly
439 found in the cytoplasm, indicating effective fractionation (Figure 2.C.5.-C.8.).
440 To further examine XIST distribution, confocal images from RNA-FISH experiments were
441 analyzed by segmenting individual cells based on DAPI signals, differentiating nuclear from
442 cytoplasmic regions. Consistent with our qPCR results, image-based intensity measurements
443 showed that both the nuclear and cytoplasmic XIST signal was significantly higher in AD
444 compared to control (Figure 2.D., 2.D.1., 2.D.2.). These findings collectively suggest that in
445 AD, XIST is not only upregulated but also undergoes a notable redistribution, shifting from its
446 typical nuclear location to an unusual presence in the cytoplasm.

447 **EZH2-XIST interaction is altered in AD, leading to reduced H3K27me3 marks on the**
448 **inactivated X chromosome**

449 The altered distribution of XIST observed in AD prompted us to explore two different aspects
450 of its function; its traditional nuclear role and a new cytoplasmic localization. We started by
451 focusing on nuclear XIST to examine its importance in the AD context.

452 In our AD model, we measured EZH2 expression at both mRNA and protein levels and found
453 it to be significantly decreased (Figure 3.A., A.1., B.). Therefore, we wanted to determine if
454 the physical interaction between EZH2 and XIST was also altered. To do this, we performed
455 RIP-qPCR with an anti-EZH2 antibody. The pull-down experiments confirmed a significant
456 reduction in XIST-EZH2 interaction in AD conditions (Figure 3.C., C1.-C3.). This spatial
457 relationship was further validated using combined immunocytochemistry (ICC) and RNA-
458 FISH with an anti-EZH2 antibody and ssDNA FISH probes targeting XIST (Figure 4.A., B.).
459 The 3D imaging analysis showed a noticeably decreased colocalization between XIST and
460 EZH2 in AD cells compared to controls (Figure 4.C.).
461 Given the impaired XIST–EZH2 interaction, subsequent investigation focused on the
462 downstream heterochromatin dynamics mediated by H3K27me3. The overall levels of
463 H3K27me3 were significantly decreased in AD (Supplementary Figure S3.). Next, three-
464 dimensional colocalization analysis was performed on z-stacks from dual-labeling experiments
465 combining H3K27me3 immunostaining with XIST RNA-FISH (Figure 5.A, B). This spatial
466 analysis revealed a substantial disruption of the XIST–H3K27me3 association in the AD
467 model. In control cells, XIST RNA foci strongly colocalized with regions enriched for
468 H3K27me3 within the nucleus, as shown in merged confocal z-projections. These colocalized
469 domains, indicated by the overlap of XIST and H3K27me3 signals, demonstrated proper
470 colocalization of XIST to the repressive chromatin compartments of the inactive X
471 chromosome, consistent with its canonical role in gene silencing (Figure 5.A.). In AD-
472 mimicking cells in contrast, although H3K27me3 puncta and nuclear XIST signal overlap
473 remained visible (Figure 5.B.)., quantitative analysis using Pearson's correlation coefficient
474 demonstrated a statistically significant decrease in XIST–H3K27me3 colocalization in AD
475 cells compared to controls (Figure 5.C).
476 These findings indicated that the loss of EZH2-XIST interaction not only signalled impaired
477 recruitment of PRC2 machinery but also hindered heterochromatin formation on Xi, potentially
478 contributing to the epigenetic instability seen in AD pathogenesis.

479 **Heightened THOC2 levels facilitate THOC2(TREX)-XIST association in AD**

480 THOC2, a protein subunit of the TREX complex and an RNA export factor, has been
481 hypothesized to play a role in the nuclear export of lncRNAs [20]. *THOC2* being X-linked, we
482 questioned whether the XIST-mediated altered nuclear epigenetic machinery could influence
483 *THOC2* promoter enrichment in AD through H3K27me3 marks.

484 To investigate any changes in the chromatin landscape of the *THOC2* promoter region, which
485 has been shown to be silenced in the human Barr body [37], ChIP-qPCR was performed. The
486 results showed that the *THOC2* proximal promoter region has a significantly higher association
487 with repressive H3K27me3 marks in AD compared to the controls (Figure 6.A., A.1., A.2.).
488 While the THOC2 mRNA levels were found to be significantly downregulated, interestingly,
489 the THOC2 protein levels were found to be significantly upregulated in AD (Figure 6.B., B.1.,
490 B.2.).
491 Next, we wanted to investigate whether this aberrant THOC2 upregulation could influence
492 THOC2-XIST interaction. The RIP-qPCR studies showed increased THOC2-XIST interaction
493 in AD compared to control (Figure 6.C., C.1.-C.3.). These results established the physical
494 interaction between the RNA export factor subunit THOC2 and XIST, which could potentially
495 facilitate the recruitment of XIST onto the TREX-mediated nuclear export machinery.
496 Next, using 3D colocalization analysis, we examined the interaction between THOC2 and
497 XIST based on ICC-FISH imaging data in both control and AD cell models (Figure 7.A., B.),
498 and we observed a higher colocalization of THOC2-XIST signals in AD compared to controls
499 (7.C.).

500 **Cytoplasmic XIST helps maintain EZH2 and THOC2 in the AD nucleus via the**
501 **miR186/XIST axis**

502 The nuclear XIST was found to be upregulated in AD compared to the control (Figure 2.C.3.).
503 However, the XIST-EZH2 association was significantly downregulated (Figure 3.C.1., 4.C.).
504 In the case of THOC2, nuclear XIST showed increased interaction in AD compared to the
505 control (Figures 6.C.1., 7.C.). Since XIST's functionality has traditionally been studied within
506 nuclear territories, its cytoplasmic fate, particularly regarding miRNA sponging, remained
507 unexplored. Previous studies have shown that the miR-186/XIST sponging interaction plays a
508 crucial role in mediating XIST-based regulation [18]. We aimed to investigate whether this axis
509 is essential for modulating XIST's nuclear functions involving EZH2/XIST and THOC2/XIST
510 associations in AD.
511 Initially, both EZH2 and THOC2 mRNAs were found to be significantly downregulated in AD
512 when XIST was knocked down (Figure 8.A.-C.). XIST-KD followed by western blots showed
513 similar trends at the protein level as well (Figure 8.D., D.1, D.2.). Thus, elevated XIST levels
514 were found to be essential in maintaining the expression levels of these two XIST-interacting
515 proteins. Next, we aimed to determine whether the maintenance of EZH2 and THOC2 proteins
516 by XIST could be mediated through its interactions with miR186.

The StarBase v2.0 database [38] search identified miR-186 binding sites in the mRNA transcripts of EZH2 and THOC2 (Figure 8.E.). In AD, miR-186 levels were significantly reduced (Figure 8.F.). Conversely, knocking down XIST in AD samples led to a significant increase in miR-186 expression (Figure 8.G.), supporting the presence of the miR-186/XIST axis in AD. When miR-186 was overexpressed (Figure 8.H.), there was a notable decrease in EZH2 and THOC2 mRNA (Figures 8.I, J) and protein (Figure 8.K., K.1., K.2) expression levels. This suggests that the miR-186/XIST axis regulates both EZH2 and THOC2 (Figure 8.L.), which then interact with XIST in the nucleus.

The mature miRNA induces post-transcriptional gene silencing via the RISC complex in the cytoplasm [39]. To further verify the novel miR186/EZH2 and miR186/THOC2 axes through cytoplasmic XIST, a biotinylated RNA pull-down experiment was performed. The miR-186 mimic with a 3' biotin modification was transfected into the AD model. The cells were then lysed, and the miR-186-interactome was isolated from the cytoplasmic fraction using streptavidin-coated magnetic beads. The interactors were identified with qPCR (Figure 9.A.). Each interaction was normalized with 10% input RNA and compared to a scrambled mimic as a negative control.

The pull-down experiment showed significantly strong interactions between miR-186 and XIST, EZH2, and THOC2, compared to the negative control in the AD cytoplasm (Figure 9.B., B.1.-B.3.). The fractionation efficiency was confirmed using SCARNA9 as a nuclear marker and tRNA as the cytoplasmic marker (Supplementary Figure S4.).

Discussion

AD continues to be a significant health issue, affecting women more than men, though the reasons remain unclear [3]. One potential contributing factor is the lncRNAs involved in regulating the disease processes [40]. These transcripts frequently exhibit inherent sex-specific biases in their expression and function [4]. The link between the lncRNA XIST and AD regulation offers new opportunities to explore the disease's underlying mechanisms [7], especially considering its sex-specific predisposition.

XIST is well-known for its function in X-chromosome inactivation. Since female cells possess an extra X chromosome compared to males, XIST inactivates this chromosome to maintain proper gene dosage across the human genome. As a result, female cells naturally show higher levels of XIST than male cells [6], [8], [9]. It has been previously reported that XIST is markedly upregulated in AD [13], a finding supported by our snRNA-seq data and qPCR

549 measurements from the AD cell model. This raises the question of whether XIST dysregulation
550 may reveal female-biased aspects of AD pathophysiology.
551 The upregulated XIST from the snRNA-seq dataset (GSE138852), along with its co-expressed
552 genes, revealed the downstream pathways impacted by this lncRNA in AD. Notably, XIST
553 appears to promote transcriptional silencing through heterochromatin formation, while also
554 decreasing functions related to synaptic transmission and protein translation. This indicates that
555 XIST might play an important role in exacerbating AD pathology. These effects could clarify
556 why higher XIST levels in females can be associated with an increased risk of AD.
557 XIST has traditionally been regarded as a nuclear-enriched RNA [41]. Recent evidence
558 suggests the presence of cytoplasmic XIST under pro-inflammatory stress conditions [17].
559 Another study has previously reported the presence of cytoplasmic XIST in AD [7]. However,
560 the functions of this cytoplasmic XIST pool remain largely unexplored. Using our cell model,
561 we performed fractionation-qPCR and RNA-FISH to quantify cytoplasmic XIST and its
562 contribution to overall XIST-mediated dysregulation. Our data indicate that in AD, both nuclear
563 and cytoplasmic XIST are significantly upregulated, with a more pronounced increase in
564 cytoplasmic XIST levels compared to nuclear XIST.
565 In the nucleus, the inactivated X chromosome (also known as the Barr body) is silenced through
566 transcriptional repression. The presence of XIST across the chromosome enables the
567 recruitment of the PRC2 complex, with the methyltransferase EZH2 as the catalytic subunit.
568 EZH2 methylates the Lysine 27 residue of H3 histone proteins in the chromatin, mediating the
569 transcriptional silencing of the chromosome [10], [11]. In AD, EZH2 levels were found to be
570 significantly reduced. When XIST is pulled down through RIP with an anti-EZH2 antibody,
571 the qPCR data suggests reduced EZH2-XIST association in AD. This could substantially
572 impact the heterochromatinization machinery of the Barr body. The 3D colocalization analyses
573 reveal altered H3K27me3 marks on the inactivated X chromosome, which would, in turn, affect
574 the X-linked genes in AD and their aberrant expression from the X chromosome in females.
575 One such X-linked gene is *THOC2*, part of the TREX complex. TREX regulates the mRNA
576 export machinery, guiding the fate of transcripts [22]. Recent reports suggest that this
577 machinery also facilitates the export of lncRNA from the nucleus [20], leading to the hypothesis
578 that, with an altered epigenetic landscape, XIST could influence the abnormal upregulation of
579 THOC2 in AD. The ChIP-qPCR studies demonstrate that the deposition of H3K27me3 on the
580 *THOC2* promoter promotes transcriptional repression of the gene. Similar trend is followed
581 with the THOC2 mRNA expression being downregulated in AD. However, at the protein level,
582 THOC2 is found to be significantly upregulated in AD. This indicates the presence of an

583 additional layer of epigenetic mechanism driving the unusual increase of THOC2 protein
584 expression. Further ChIP-qPCR studies targeting H3K4me3 and H3K27ac could help explore
585 how these chromatin modifiers affect the transcriptional activity of the *THOC2* promoter. The
586 RIP-qPCR studies targeting THOC2 protein show that XIST interacts strongly with THOC2,
587 suggesting a novel XIST/TREX RNA-protein complex. Thus, for the first time, XIST can be
588 linked with the nuclear RNA export pathways. It can further be hypothesized that this
589 interaction may play an essential role in XIST's own nuclear export.
590 One of the most important pathways through which lncRNAs confer their functions is by
591 sponging miRNAs [42]. The miRNA-186 has been previously reported to suppress BACE1,
592 potentially suppressing the amyloidogenic pathways [19]. The expression of this miRNA is
593 downregulated in AD. Previously, the miR186/XIST axis has been validated through luciferase
594 assays in cancer [18]. However, how this axis would act in a neurodegenerative scenario was
595 of significant interest. Furthermore, the role of cytoplasmic XIST in AD being unclear, it was
596 of considerable interest to see whether the cytoplasmic XIST pool interacts with miR-186 in
597 AD to perform its neurodegenerative functions. The miRNA pull-down studies from the
598 cytoplasmic fraction revealed XIST's significant association with miR-186 in the cytoplasm
599 and the presence of two novel targets of miR-186, viz., EZH2 and THOC2. Upregulating miR-
600 186 downregulated both these genes, while XIST knockdown upregulated miR-186 levels,
601 resulting in the downregulation of both EZH2 and THOC2. While the nuclear H3K27me3
602 marks on the *THOC2* promoter drive its downregulation in AD, the significant downregulation
603 of miR-186 by XIST in AD could partially outweigh the nuclear transcriptional repression,
604 contributing to the overall upregulation of THOC2 protein in AD.
605 miRNA-mediated RNA silencing has traditionally been shown to occur in the cytoplasm [43].
606 The presence of XIST in the cytoplasmic compartment in AD sequesters miR-186, preventing
607 the degradation of both EZH2 and THOC2 mRNA. Therefore, cytoplasmic XIST, through
608 miR-186, maintains the nuclear pool of EZH2 and THOC2 proteins for nuclear XIST's
609 functions in AD.

610 **Conclusion**

611 Our research uncovers a dual function of XIST in AD. Inside the nucleus, it facilitates
612 epigenetic silencing, while in the cytoplasm, it affects miRNA availability, supporting the
613 expression of key regulatory proteins. This twofold role may partly explain why AD is more
614 common in women, as higher XIST levels could contribute to increased molecular imbalance.
615 By identifying these linked regulatory pathways, the study deepens our understanding of sex-

specific mechanisms in AD and highlights XIST as a promising target for neurodegenerative disease treatment.

References

[1] P. T. Kamatham, R. Shukla, D. K. Khatri, and L. K. Vora, 'Pathogenesis, diagnostics, and therapeutics for Alzheimer's disease: Breaking the memory barrier', *Ageing Res Rev*, vol. 101, p. 102481, Nov. 2024, doi: 10.1016/J.ARR.2024.102481.

[2] M. Cao, H. Li, J. Zhao, J. Cui, and G. Hu, 'Identification of age- and gender-associated long noncoding RNAs in the human brain with Alzheimer's disease', *Neurobiol Aging*, vol. 81, pp. 116–126, Sep. 2019, doi: 10.1016/J.NEUROBIOLAGING.2019.05.023.

[3] C. Lopez-Lee, E. R. S. Torres, G. Carling, and L. Gan, 'Mechanisms of sex differences in Alzheimer's disease', *Neuron*, vol. 112, no. 8, pp. 1208–1221, Apr. 2024, doi: 10.1016/J.NEURON.2024.01.024.

[4] M. Cao, H. Li, J. Zhao, J. Cui, and G. Hu, 'Identification of age- and gender-associated long noncoding RNAs in the human brain with Alzheimer's disease', *Neurobiol Aging*, vol. 81, p. 116, Sep. 2019, doi: 10.1016/J.NEUROBIOLAGING.2019.05.023.

[5] S. Sen and D. Mukhopadhyay, 'A Holistic Analysis of Alzheimer's Disease-Associated lncRNA Communities Reveals Enhanced lncRNA-miRNA-RBP Regulatory Triad Formation Within Functionally Segregated Clusters', *Journal of Molecular Neuroscience*, vol. 74, no. 3, pp. 1–27, Sep. 2024, doi: 10.1007/S12031-024-02244-0/FIGURES/8.

[6] E. C. Jacobson, A. Pandya-Jones, and K. Plath, 'A lifelong duty: how Xist maintains the inactive X chromosome', *Curr Opin Genet Dev*, vol. 75, p. 101927, Aug. 2022, doi: 10.1016/J.GDE.2022.101927.

[7] X. W. Yan, H. J. Liu, Y. X. Hong, T. Meng, J. Du, and C. Chang, 'lncRNA XIST induces Aβ accumulation and neuroinflammation by the epigenetic repression of NEP in Alzheimer's disease', *J Neurogenet*, vol. 36, no. 1, pp. 11–20, 2022, doi: 10.1080/01677063.2022.2028784.

[8] A. Sahakyan, Y. Yang, and K. Plath, 'The role of Xist in X-chromosome dosage compensation', *Trends Cell Biol*, vol. 28, no. 12, p. 999, Dec. 2018, doi: 10.1016/J.TCB.2018.05.005.

[9] C. Morey, C. Rougeulle, and J. F. Ouimette, 'Unleashing XIST from X-chromosome inactivation', *Curr Opin Cell Biol*, vol. 92, p. 102446, Feb. 2025, doi: 10.1016/J.CEB.2024.102446.

[10] K. Sarma *et al.*, 'ATRX Directs Binding of PRC2 to Xist RNA and Polycomb Targets', *Cell*, vol. 159, no. 4, pp. 869–883, Nov. 2014, doi: 10.1016/J.CELL.2014.10.019.

[11] E. Maclary, M. Hinten, C. Harris, S. Sethuraman, S. Gayen, and S. Kalantry, 'PRC2 represses transcribed genes on the imprinted inactive X chromosome in mice', *Genome Biol*, vol. 18, no. 1, pp. 1–17, May 2017, doi: 10.1186/S13059-017-1211-5/FIGURES/6.

[12] Y. Ma *et al.*, 'LncRNA XIST regulates breast cancer stem cells by activating proinflammatory IL-6/STAT3 signaling', *Oncogene 2023 42:18*, vol. 42, no. 18, pp. 1419–1437, Mar. 2023, doi: 10.1038/s41388-023-02652-3.

[13] D. Yue *et al.*, 'Silencing of long noncoding RNA XIST attenuated Alzheimer's disease-related BACE1 alteration through miR-124', *Cell Biol Int*, vol. 44, no. 2, pp. 630–636, Feb. 2020, doi: 10.1002/cbin.11263.

[14] R. Jiang *et al.*, 'Inhibition of long non-coding RNA XIST upregulates microRNA-149-3p to repress ovarian cancer cell progression', *Cell Death & Disease 2021 12:2*, vol. 12, no. 2, pp. 1–12, Feb. 2021, doi: 10.1038/s41419-020-03358-0.

[15] M. Wozniak and M. Czyz, 'lncRNAs-EZH2 interaction as promising therapeutic target in cutaneous melanoma', *Front Mol Biosci*, vol. 10, p. 1170026, May 2023, doi: 10.3389/FMOLB.2023.1170026/PDF.

[16] T. Xu *et al.*, 'Upregulation of long noncoding RNA Xist promotes proliferation of osteosarcoma by epigenetic silencing of P21', *Oncotarget*, vol. 8, no. 60, pp. 101406–101417, Sep. 2017, doi: 10.18632/ONCOTARGET.20738.

[17] B. B. Shenoda *et al.*, 'Xist attenuates acute inflammatory response by female cells', *Cell Mol Life Sci*, vol. 78, no. 1, pp. 299–316, Jan. 2021, doi: 10.1007/S00018-020-03500-3.

[18] H. Wang *et al.*, 'The Long Non-Coding RNA XIST Controls Non-Small Cell Lung Cancer Proliferation and Invasion by Modulating miR-186-5p', *Cellular Physiology and Biochemistry*, vol. 41, no. 6, pp. 2221–2229, Jun. 2017, doi: 10.1159/000475637.

[19] J. Kim, H. Yoon, D. E. Chung, J. L. Brown, K. C. Belmonte, and J. Kim, 'miR-186 is decreased in aged brain and suppresses BACE1 expression', *J Neurochem*, vol. 137, no. 3, p. 436, May 2016, doi: 10.1111/JNC.13507.

[20] B. Zuckerman, M. Ron, M. Mikl, E. Segal, and I. Ulitsky, 'Gene Architecture and Sequence Composition Underpin Selective Dependency of Nuclear Export of Long RNAs on NXF1 and the TREX Complex', *Mol Cell*, vol. 79, no. 2, pp. 251-267.e6, Jul. 2020, doi: 10.1016/J.MOLCEL.2020.05.013/ASSET/82F175F3-5CE4-4D99-A743-EBED51552D50/MAIN.ASSETS/GR7.JPG.

[21] H. R. Cohen and B. Panning, 'XIST RNA exhibits nuclear retention and exhibits reduced association with the export factor TAP/NXF1', *Chromosoma*, vol. 116, no. 4, pp. 373–383, Aug. 2007, doi: 10.1007/s00412-007-0100-1.

[22] R. Bhattacharjee *et al.*, 'Compromised transcription-mRNA export factor THOC2 causes R-loop accumulation, DNA damage and adverse

696 neurodevelopment', *Nat Commun*, vol. 15, no. 1, pp. 1–25, Dec. 2024, doi:
697 10.1038/S41467-024-45121-5;TECHMETA.

698 [23] R. Edgar, M. Domrachev, and A. E. Lash, 'Gene Expression Omnibus: NCBI
699 gene expression and hybridization array data repository', *Nucleic Acids Res*,
700 vol. 30, no. 1, pp. 207–210, Jan. 2002, doi: 10.1093/NAR/30.1.207.

701 [24] V. D. Blondel, J. L. Guillaume, R. Lambiotte, and E. Lefebvre, 'Fast unfolding
702 of communities in large networks', *Journal of Statistical Mechanics: Theory*
703 *and Experiment*, vol. 2008, no. 10, Mar. 2008, doi: 10.1088/1742-
704 5468/2008/10/p10008.

705 [25] J. W. Squair *et al.*, 'Confronting false discoveries in single-cell differential
706 expression', *Nat Commun*, vol. 12, no. 1, pp. 1–15, Dec. 2021, doi:
707 10.1038/S41467-021-25960-2;TECHMETA.

708 [26] T. Wu *et al.*, 'clusterProfiler 4.0: A universal enrichment tool for interpreting
709 omics data', *The Innovation*, vol. 2, no. 3, p. 100141, Aug. 2021, doi:
710 10.1016/J.XINN.2021.100141.

711 [27] R. A. M. Villanueva and Z. J. Chen, 'ggplot2: Elegant Graphics for Data
712 Analysis (2nd ed.)', *Measurement (Mahwah N J)*, vol. 17, no. 3, pp. 160–167,
713 Jul. 2019, doi: 10.1080/15366367.2019.1565254.

714 [28] M. Raychaudhuri and D. Mukhopadhyay, 'Grb2-Mediated Alteration in the
715 Trafficking of AβPP: Insights from Grb2-AICD Interaction', *Journal of*
716 *Alzheimer's Disease*, vol. 20, no. 1, pp. 275–292, Jan. 2010, doi: 10.3233/JAD-
717 2010-1371.

718 [29] M. Raychaudhuri and D. Mukhopadhyay, 'AICD and its adaptors - in search of
719 new players', *J Alzheimers Dis*, vol. 11, no. 3, pp. 343–358, 2007, doi:
720 10.3233/JAD-2007-11311.

721 [30] S. Baksi, N. R. Jana, N. P. Bhattacharyya, and D. Mukhopadhyay, 'Grb2 Is
722 Regulated by Foxd3 and Has Roles in Preventing Accumulation and
723 Aggregation of Mutant Huntingtin', *PLoS One*, vol. 8, no. 10, p. e76792, Oct.
724 2013, doi: 10.1371/JOURNAL.PONE.0076792.

725 [31] K. Roy, M. Raychaudhuri, O. Chakrabarti, and D. Mukhopadhyay, 'Growth
726 Factor Receptor-Bound Protein 2 Promotes Autophagic Removal of Amyloid-β
727 Protein Precursor Intracellular Domain Overload in Neuronal Cells', *Journal of*
728 *Alzheimer's Disease*, vol. 38, no. 4, pp. 881–895, Jan. 2014, doi: 10.3233/JAD-
729 130929.

730 [32] P. Majumder, K. Roy, B. K. Singh, N. R. Jana, and D. Mukhopadhyay, 'Cellular
731 levels of Grb2 and cytoskeleton stability are correlated in a neurodegenerative
732 scenario', *DMM Disease Models and Mechanisms*, vol. 10, no. 5, pp. 655–669,
733 May 2017, doi: 10.1242/DMM.027748/257113/AM/CELLULAR-LEVELS-
734 OF-GROWTH-FACTOR-RECEPTOR-BOUND.

735 [33] K. Chanda, N. R. Jana, and D. Mukhopadhyay, 'Receptor tyrosine kinase ROR1
736 ameliorates Aβ1–42 induced cytoskeletal instability and is regulated by the

miR146a-NEAT1 nexus in Alzheimer's disease', *Scientific Reports 2021 11:1*, vol. 11, no. 1, pp. 1–15, Sep. 2021, doi: 10.1038/s41598-021-98882-0.

[34] M. F. Kramer, 'STEM-LOOP RT-qPCR for miRNAS', *Current protocols in molecular biology / edited by Frederick M. Ausubel ... [et al.]*, vol. CHAPTER, no. SUPPL. 95, p. Unit15.10, 2011, doi: 10.1002/0471142727.MB1510S95.

[35] J. Schindelin *et al.*, 'Fiji: An open-source platform for biological-image analysis', *Nat Methods*, vol. 9, no. 7, pp. 676–682, Jul. 2012, doi: 10.1038/NMETH.2019;SUBJMETA=1647,245,631,794;KWRD=IMAGING,SOFTWARE.

[36] P. Phatak and J. M. Donahue, 'Biotinylated Micro-RNA Pull Down Assay for Identifying miRNA Targets', *Bio Protoc*, vol. 7, no. 9, p. e2253, 2017, doi: 10.21769/BIOPROTOC.2253.

[37] T. Tukiainen *et al.*, 'Landscape of X chromosome inactivation across human tissues', *Nature*, vol. 550, no. 7675, pp. 244–248, Oct. 2017, doi: 10.1038/NATURE24265;TECHMETA.

[38] J. H. Li, S. Liu, H. Zhou, L. H. Qu, and J. H. Yang, 'starBase v2.0: decoding miRNA-ceRNA, miRNA-ncRNA and protein–RNA interaction networks from large-scale CLIP-Seq data', *Nucleic Acids Res*, vol. 42, no. D1, pp. D92–D97, Jan. 2014, doi: 10.1093/NAR/GKT1248.

[39] H. Liu, C. Lei, Q. He, Z. Pan, D. Xiao, and Y. Tao, 'Nuclear functions of mammalian MicroRNAs in gene regulation, immunity and cancer', *Mol Cancer*, vol. 17, no. 1, Feb. 2018, doi: 10.1186/S12943-018-0765-5.

[40] X. Wu, P. Xia, L. Yang, C. Lu, and Z. Lu, 'The roles of long non-coding RNAs in Alzheimer's disease diagnosis, treatment, and their involvement in Alzheimer's disease immune responses', *Noncoding RNA Res*, vol. 9, no. 3, pp. 659–666, Sep. 2024, doi: 10.1016/J.NCRNA.2024.03.008.

[41] I. Jonkers, K. Monkhorst, E. Rentmeester, J. A. Grootegoed, F. Grosveld, and J. Gribnau, 'Xist RNA Is Confined to the Nuclear Territory of the Silenced X Chromosome throughout the Cell Cycle', *Mol Cell Biol*, vol. 28, no. 18, p. 5583, Sep. 2008, doi: 10.1128/MCB.02269-07.

[42] Y. Du *et al.*, 'LncRNA XIST acts as a tumor suppressor in prostate cancer through sponging miR-23a to modulate RKIP expression', *Oncotarget*, vol. 8, no. 55, pp. 94358–94370, Nov. 2017, doi: 10.18632/oncotarget.21719.

[43] A. K. L. Leung, 'The Whereabouts of miRNA Actions: Cytoplasm and Beyond', *Trends Cell Biol*, vol. 25, no. 10, p. 601, Oct. 2015, doi: 10.1016/J.TCB.2015.07.005.

Data Availability

The dataset used in this study is publicly accessible at the NCBI Gene Expression Omnibus (https://www.ncbi.nlm.nih.gov/geo/). The R scripts used to analyze the data can be provided with reasonable request.

Acknowledgements

SS acknowledges fellowship support from the Saha Institute of Nuclear Physics (Government of India). Illustrations were Created with BioRender.com.

Funding

This work was supported by the Department of Atomic Energy, Government of India (RSI 4002), and by a Core Research Grant from the Department of Science and Technology–Science and Engineering Research Board (DST-SERB), Government of India (CRG/2021/000678).

Conflict of Interest

The authors declare no competing interests.

Author Contributions

DM supervised the project and secured funding. SS and DM jointly conceived and designed the study. SS performed experiments, conducted data analysis, prepared figures and illustrations, and drafted the manuscript. DM reviewed and edited the manuscript.

803 **Figures**

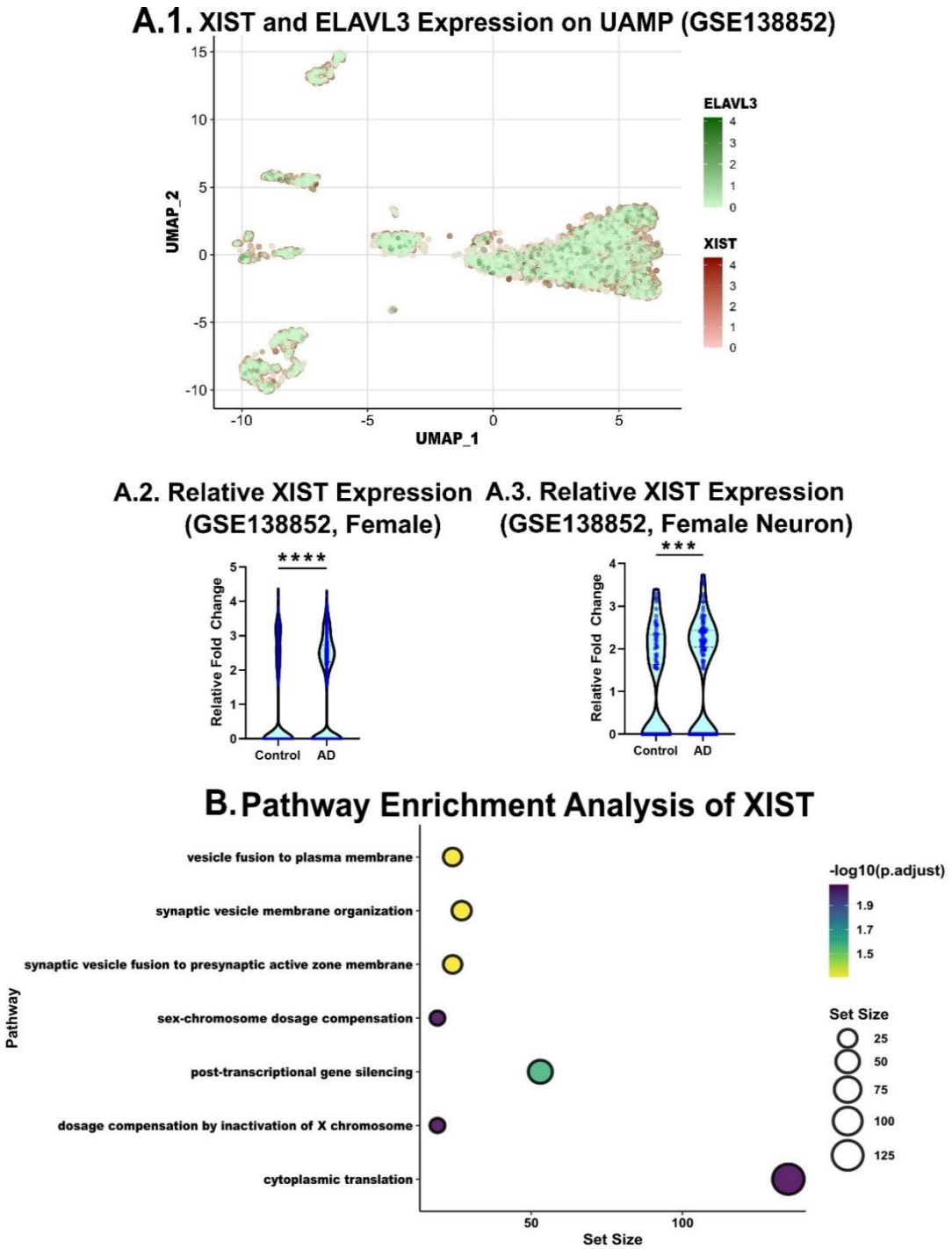

804

805 ***Figure 1. (A.1) UMAP projection showing colocalization of XIST expression with neuronal***
806 ***nuclei in female cells. (A.2) The differential expression analysis across various cell nuclei***
807 ***populations revealed significant upregulation of XIST in females. (A.3) The neuronal***
808 ***subpopulations of the female subset showed significant upregulation of XIST in AD. (B.)***
809 ***GSEA results indicating pathways associated with aberrant XIST expression in AD neurons.***

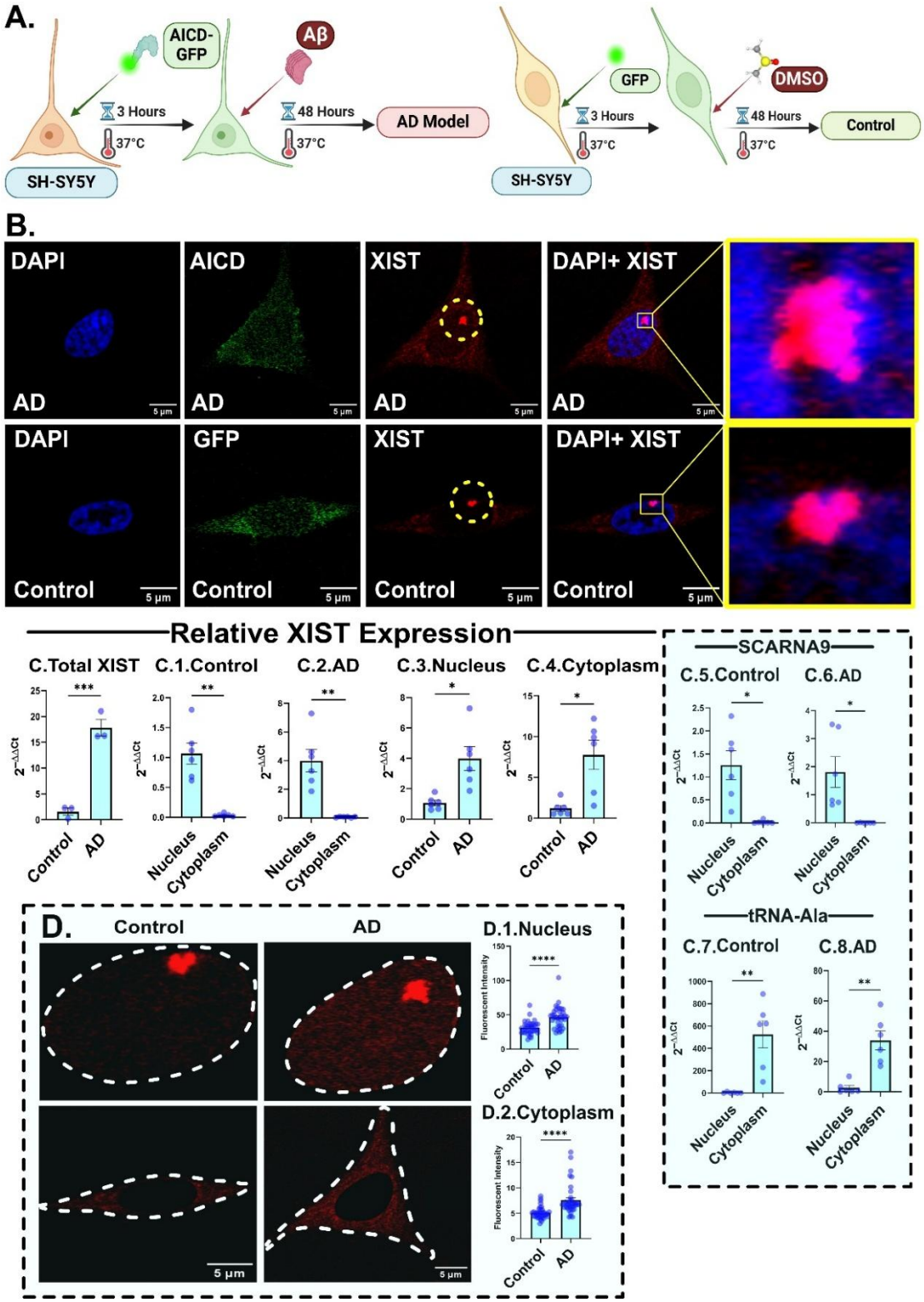

Figure 2. XIST Ectopic Distribution in AD Cell Model. (A) Schematic of the experimental workflow. SH-SY5Y neuroblastoma cells were transfected with AICD-GFP or GFP constructs and incubated for 3 hours at 37°C, then treated with Aβ peptide (AD model) or DMSO (control) for 48 hours. (B) Confocal images showing subcellular localization of XIST RNA (bright red punctum) in AD and control cells. DAPI (blue) stains nuclei. AICD-GFP

816 ***or GFP (green) indicates successful transfection. Colocalization of XIST with nuclear DAPI***
817 ***is visible in both conditions. In the AD model, XIST shows higher nuclear and enrichment***
818 ***compared to controls. Right panels provide zoomed-in views of XIST-DAPI overlap. (C., C.1–***
819 ***C.4) XIST was significantly upregulated in AD and mainly localized in the nucleus. Both***
820 ***nuclear and cytoplasmic fractions contained significantly higher XIST levels in AD***
821 ***compared to controls. (C.5–C.8) RT-qPCR assessment of relative nuclear versus cytoplasmic***
822 ***expression of small ncRNAs SCARNA9 and tRNA under control and AD conditions***
823 ***confirmed efficient fractionation. (D., D.1., D.2) Quantification of XIST signal intensity in***
824 ***nuclear and cytoplasmic compartments revealed elevated signals in both the nuclear and***
825 ***cytoplasmic compartments in AD. Fold change data are shown as $2^{-\Delta\Delta Ct}$; bars indicate mean***
826 ***± SEM. *p < 0.05, **p < 0.01, ***p <0.001, ****p <0.0001 (unpaired t-test).***

827

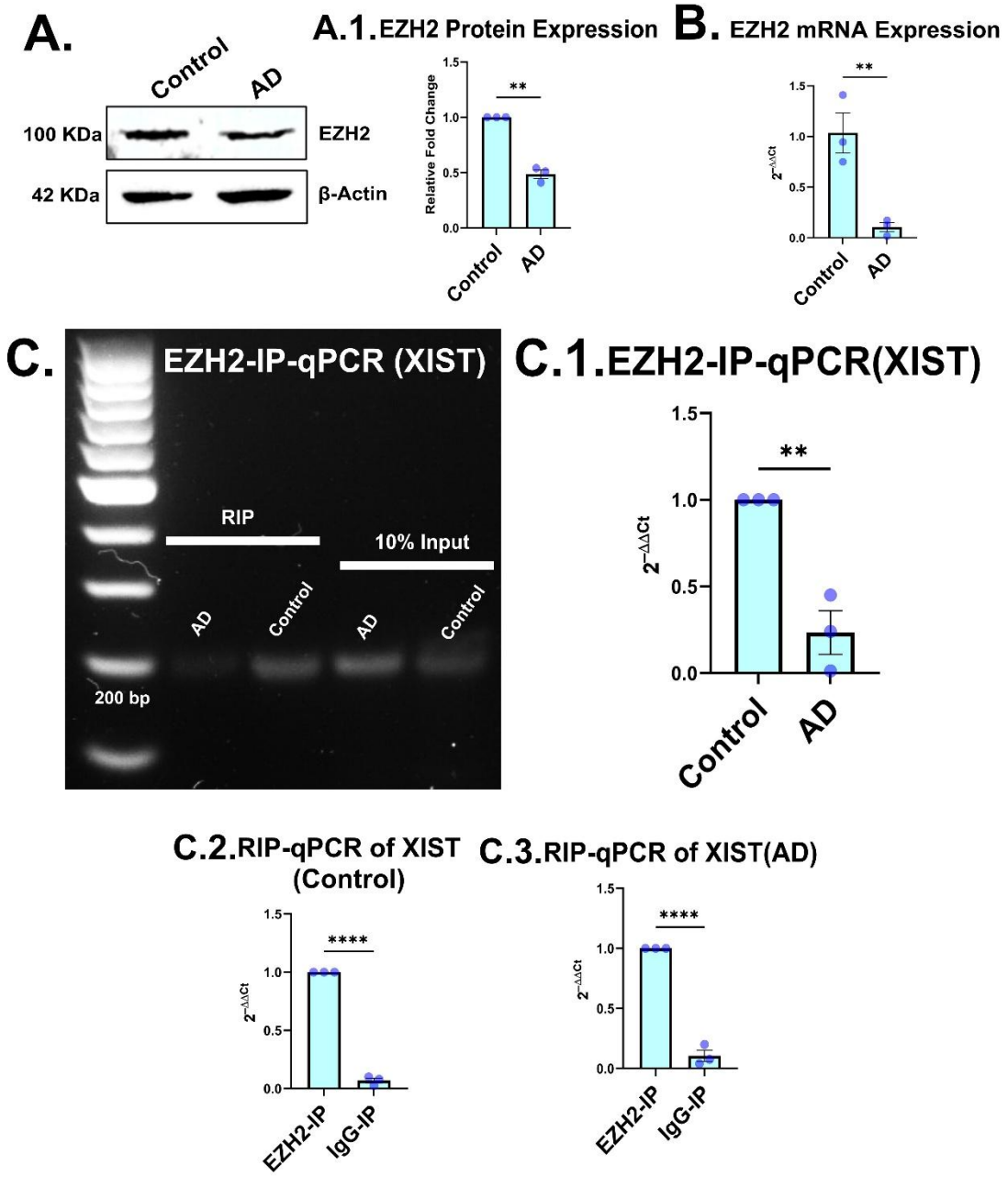

Figure 3. Impaired EZH2 expression and disrupted EZH2-XIST interaction in AD. (A) Representative immunoblot showing reduced EZH2 protein expression in AD-treated cells compared to controls. β-Actin served as the loading control. (A.1) Quantification of EZH2 protein levels revealed a significant decrease in AD-treated cells (**p < 0.01). (B) qRT-PCR analysis indicated a significant reduction in EZH2 mRNA transcription in AD-treated cells relative to control (**p < 0.01). (C)-(C.1) RIP-qPCR confirmed a significant decrease in XIST RNA bound to EZH2 in AD-treated cells compared to controls (**p < 0.01). (C.2) Enrichment of XIST RNA in EZH2-IP versus IgG-IP in GFP+DMSO-treated control cells validated assay specificity (**p < 0.0001). (C.3) Similarly, AICD+Aβ-treated AD cells showed

838 ***a significantly higher enrichment of XIST in EZH2-IP compared to IgG-IP ($p < 0.0001$),***
839 ***further confirming disrupted XIST-EZH2 interaction under AD conditions. Error bars***
840 ***indicate mean ± SEM; significance levels were determined using an unpaired Student's t***
841 ***test.***

842

843

844

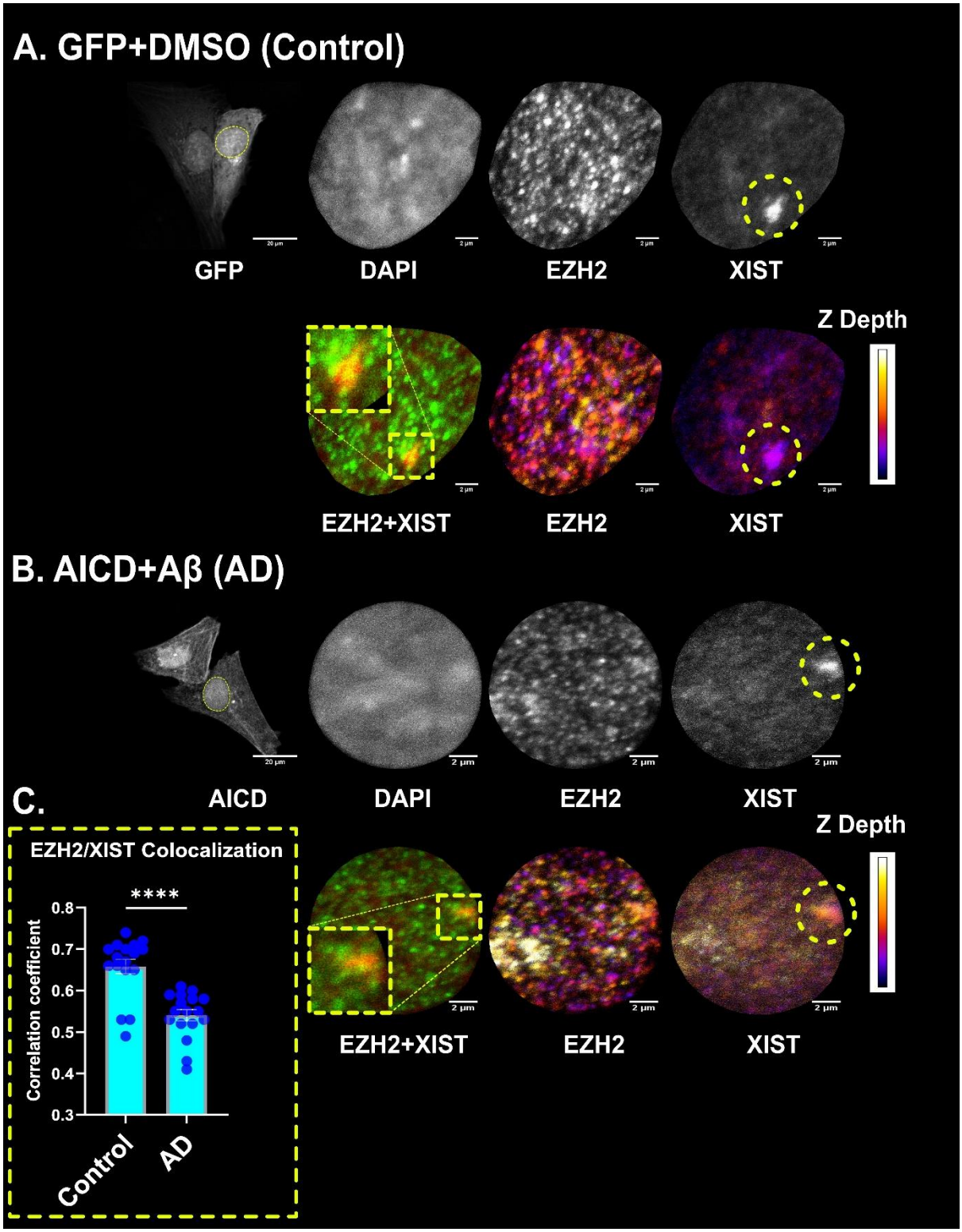

845

846 ***Figure 4. Colocalization between EZH2 and XIST is significantly reduced in AD. (A)***
847 ***Confocal images of control cells are shown, where EZH2 and XIST RNA are localized within***
848 ***the nucleus. Strong colocalization between EZH2 and XIST is seen in the merged image***
849 ***(EZH2+XIST). Nuclei were counterstained with DAPI (gray). Z-depth color coding was used***
850 ***to show spatial distribution along the axial plane, across which colocalization of the signal***

851 ***intensities was examined. (B) In AICD+Aβ-treated cells, there is reduced colocalization***
852 ***between EZH2 and XIST. (C) Pearson's correlation coefficient analysis shows a significant***
853 ***decrease in EZH2–XIST colocalization in the AD group compared to control (****p <***
854 ***0.0001), indicating impaired interaction between XIST and EZH2 in the AD model. Error***
855 ***bars represent mean ± SEM.***

856

857

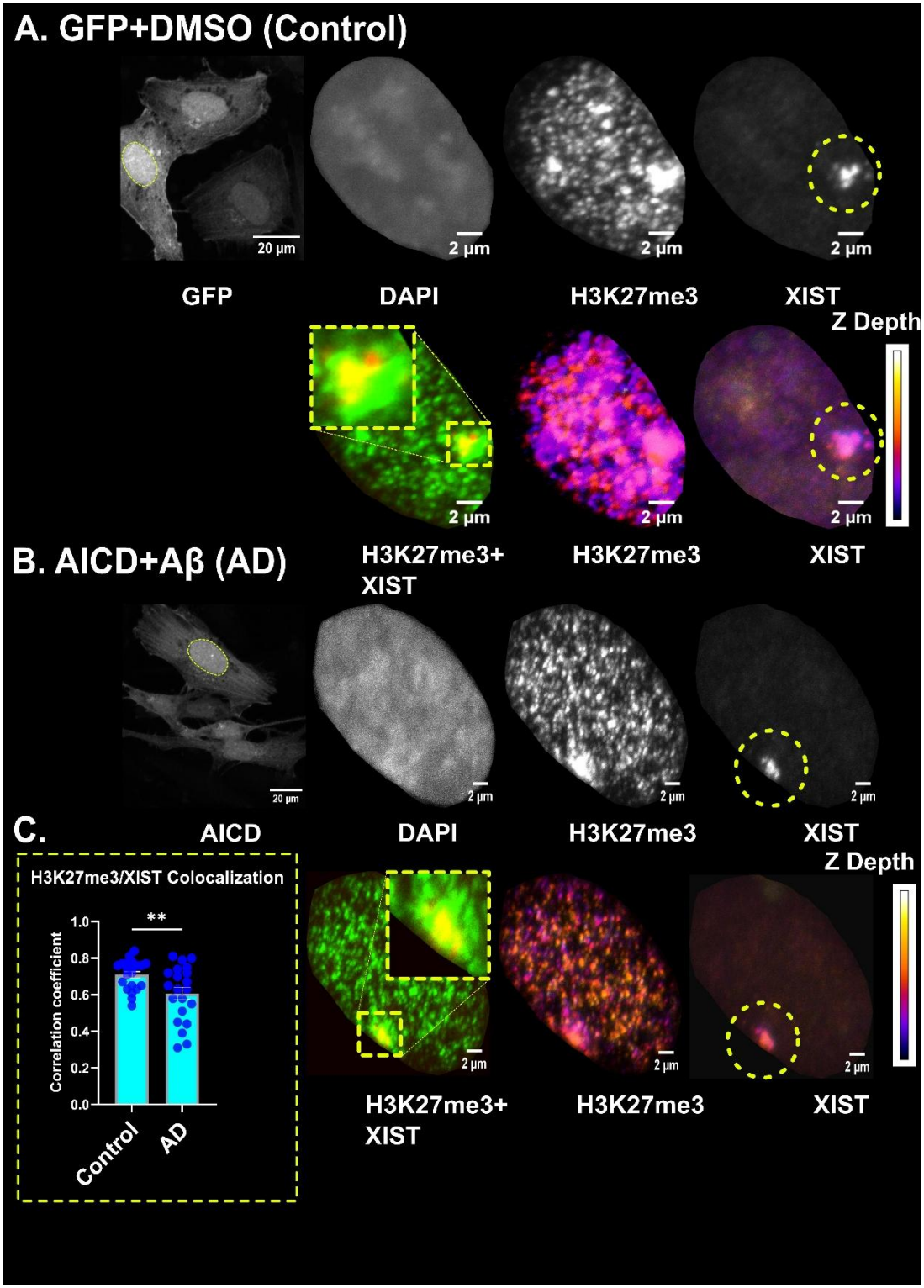

858

859 *Figure 5. Impaired colocalization of XIST with H3K27me3 in AD. (A) Confocal images of*
860 *control-treated cells showing strong nuclear colocalization between XIST RNA and*
861 *H3K27me3, a repressive histone modification catalyzed by EZH2. DAPI staining was used*
862 *to visualize nuclei. The merged panel (H3K27me3+XIST) displays a high degree of spatial*
863 *overlap, highlighted in the magnified inset. Z-depth color coding reflects axial positioning*

within the nucleus. (B) In AD-treated cells, there is a notable reduction in XIST–H3K27me3 colocalization, despite both signals being present within the nucleus. The inset represents the comparatively diminished colocalization between the two signals under AD conditions, however both these signals still show substantially detectable overlap. (C) Quantitative analysis of colocalization using Pearson's correlation coefficient confirms a statistically significant decrease in the association between XIST and H3K27me3 in the AD group compared to controls (**p < 0.01), indicating disrupted recruitment of H3K27me3 to the X chromosome in AD. Error bars represent mean ± SEM.

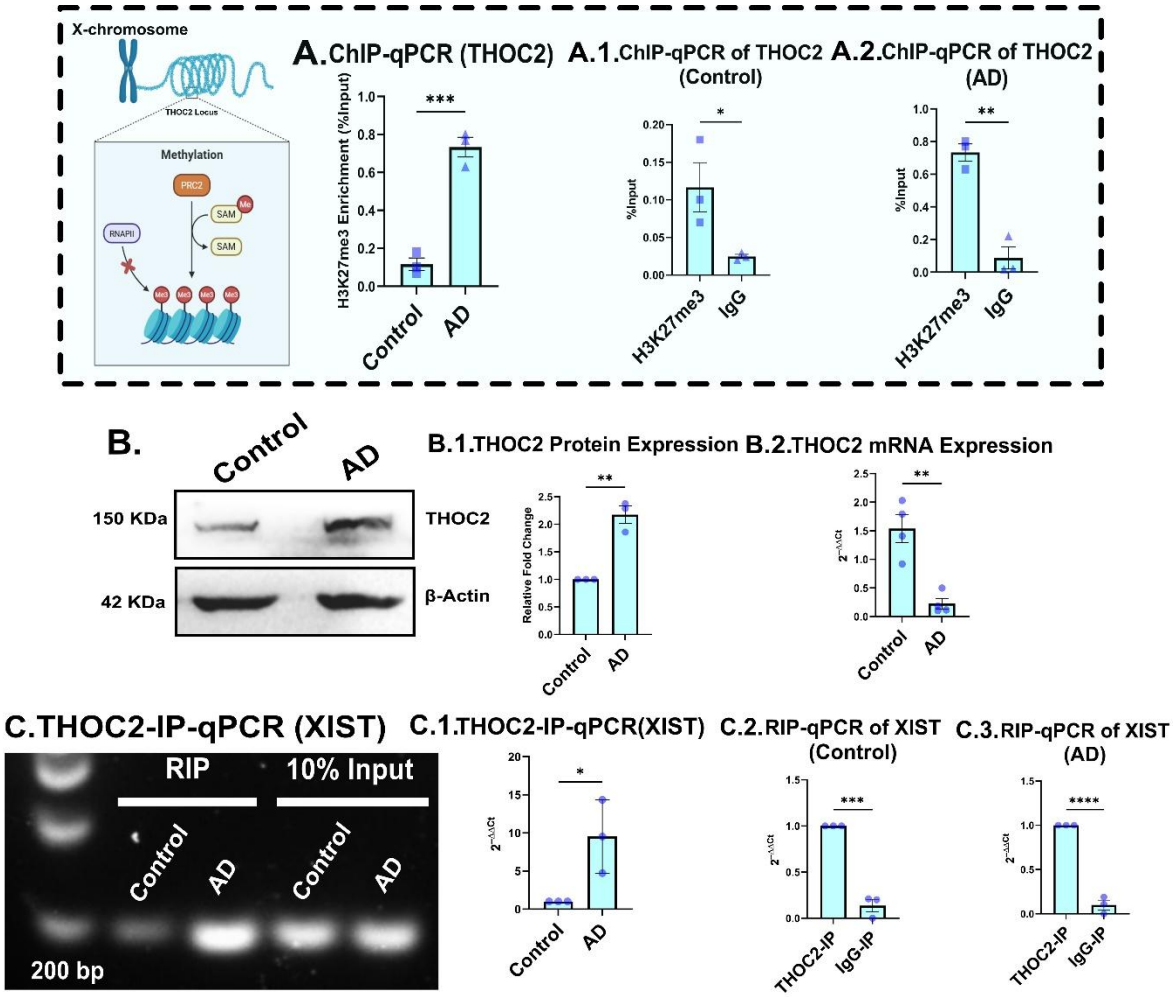

Figure 6. Upregulation of THOC2 and increased XIST–THOC2 interaction in AD. (A) ChIP-qPCR analysis showing increased H3K27me3 enrichment at the THOC2 promoter in AICD+Aβ-treated AD cells compared to GFP+DMSO-treated controls (p < 0.001). (A.1–A.2) ChIP-qPCR plots showing specific enrichment of H3K27me3 compared to IgG under GFP+DMSO (control) (*p < 0.05) and AICD+Aβ (AD) (**p < 0.01) conditions. (B) Immunoblot of THOC2 protein expression in control and AD-treated cells, with β-Actin as loading control. (B.1) Quantification revealed significant upregulation of THOC2 protein in AD-treated cells (**p < 0.01). (B.2) qRT-PCR analysis of THOC2 mRNA expression indicated a significant decrease in AD relative to control (**p < 0.01). (C) RIP-qPCR demonstrating enhanced association between THOC2 and XIST in AD. Representative gel electrophoresis image showing increased XIST enrichment in THOC2-IP from AD samples compared to controls. (C.1-C.3) qPCR quantification confirmed significant elevation of XIST binding to THOC2 in AICD+Aβ cells (*p < 0.05). The pull-down specificity validated***

892 ***by robust enrichment of XIST RNA in THOC2-IP compared to IgG-IP in both control (***p***
893 ***< 0.001) and AD (****p < 0.0001) groups. Error bars represent mean ± SEM; significance***
894 ***determined using unpaired Student's t test.***

895

896

897

898

899

900

901

902

903

904

905

906

907

908

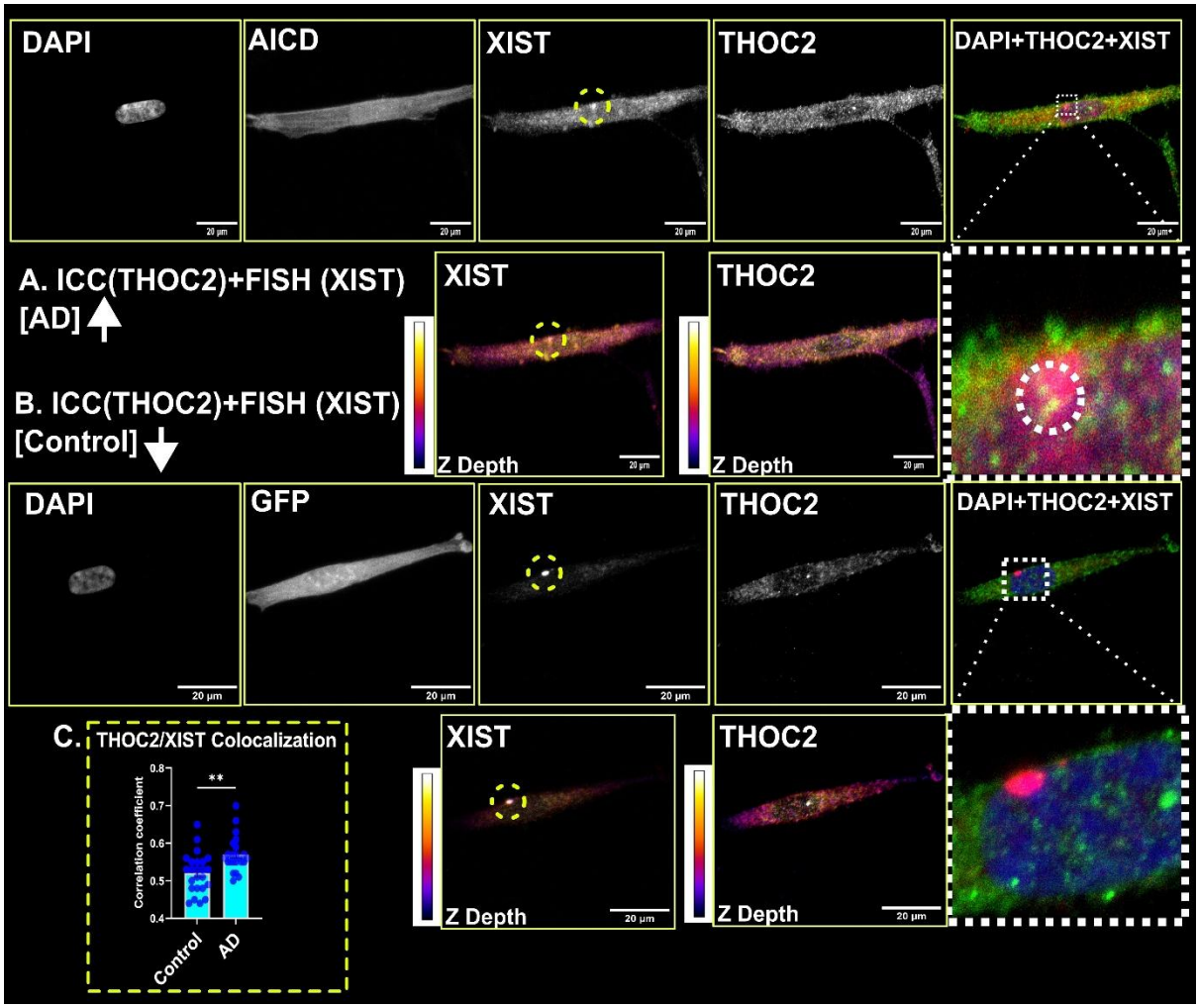

*Figure 7. Colocalization of THOC2 with XIST in AD using combined ICC and RNA FISH. The images show the spatial relationship between the lncRNA XIST and THOC2 in AD (A) and control (B) samples. Nuclei were stained with DAPI, while AICD or GFP was transfected into the AD and control cells, respectively. XIST was visualized by RNA FISH, and THOC2 was detected through ICC. Notably, in AD cells (A), XIST displays a significant increase in colocalization with THOC2, as seen in merged images, especially in the nuclear area (dotted circles, enlarged panels). Conversely, control cells (B) show much weaker colocalization signals. These findings support a possible AD-specific interaction between XIST and THOC2 within the nuclear compartment. (C) Quantitative analysis of colocalization using Pearson's correlation coefficient confirms a statistically significant increase in the association between XIST and THOC2 in the AD group compared to controls (**$p < 0.01$), indicating elevated recruitment of XIST to the TREX-mediated RNA export pathway in AD. Error bars represent mean ± SEM.*

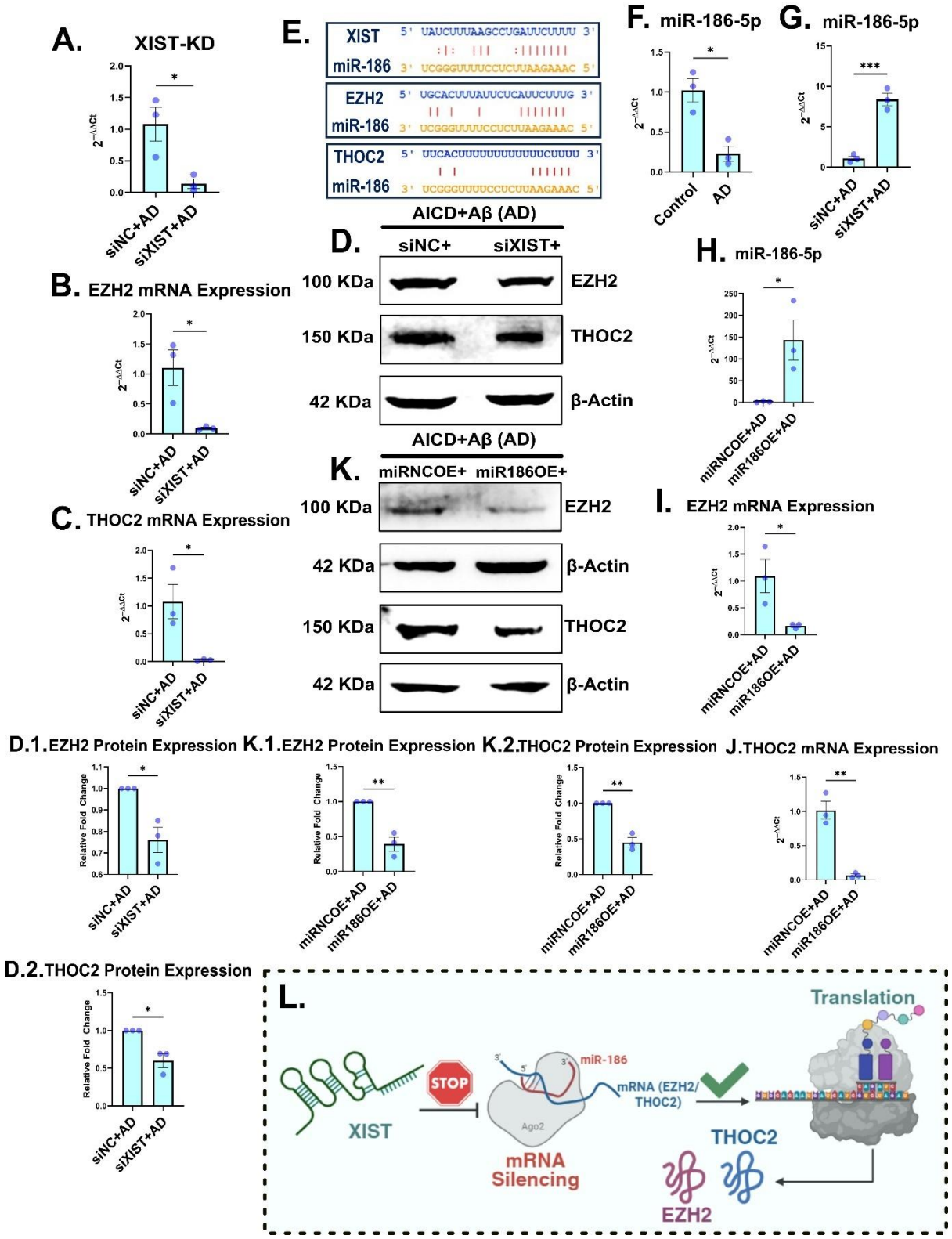

924

925 ***Figure 8. XIST–miR-186 axis regulates EZH2 and THOC2 expression in an Alzheimer's***
926 ***disease (AD) model. (A) qRT-PCR confirmed effective knockdown of XIST in AD***
927 ***(AICD+Aβ) cells, validating siXIST-mediated suppression (*p < 0.05). (B–C) XIST***
928 ***knockdown caused significant decreases in EZH2 and THOC2 mRNA levels in AD cells (*p***

929 *< 0.05). (D) Immunoblotting after siXIST treatment showed reduced EZH2 and THOC2*
930 *protein levels, with quantification confirming significant reductions in both (*p < 0.05; D.1–*
931 *D.2). β-Actin served as a loading control. (E) StarBase predicted binding sites of miR-186*
932 *on XIST, EZH2, and THOC2 transcripts. (F–G) qRT-PCR indicated that miR-186-5p*
933 *expression was lower in AD cells compared to control (*p < 0.05) and increased significantly*
934 *with XIST knockdown (***p < 0.001). (H) miR-186 overexpression (miR186OE) in AD cells*
935 *significantly increased miR-186 levels. (I–J) qRT-PCR confirmed significant decreases in*
936 *EZH2 (*p < 0.05) and THOC2 (**p < 0.01) mRNA levels following miR-186 overexpression.*
937 *(K) Immunoblotting after miR-186 overexpression revealed notable decreases in EZH2 and*
938 *THOC2 proteins, with quantification showing significant reductions in EZH2 (K.1, **p <*
939 *0.01) and THOC2 (K.2, **p < 0.01) compared to miR-NC controls. (L) Schematic diagram*
940 *depicting the proposed mechanism: XIST acts as a sponge for miR-186, preventing miR-*
941 *186-mediated silencing of EZH2 and THOC2. Depletion of XIST or overexpression of miR-*
942 *186 releases this repression, resulting in mRNA silencing and decreased protein production.*
943 *Error bars represent mean ± SEM; significance was determined using an unpaired Student's*
944 *t test.*

945

946

947

948

949

950

951

952

953

954

955

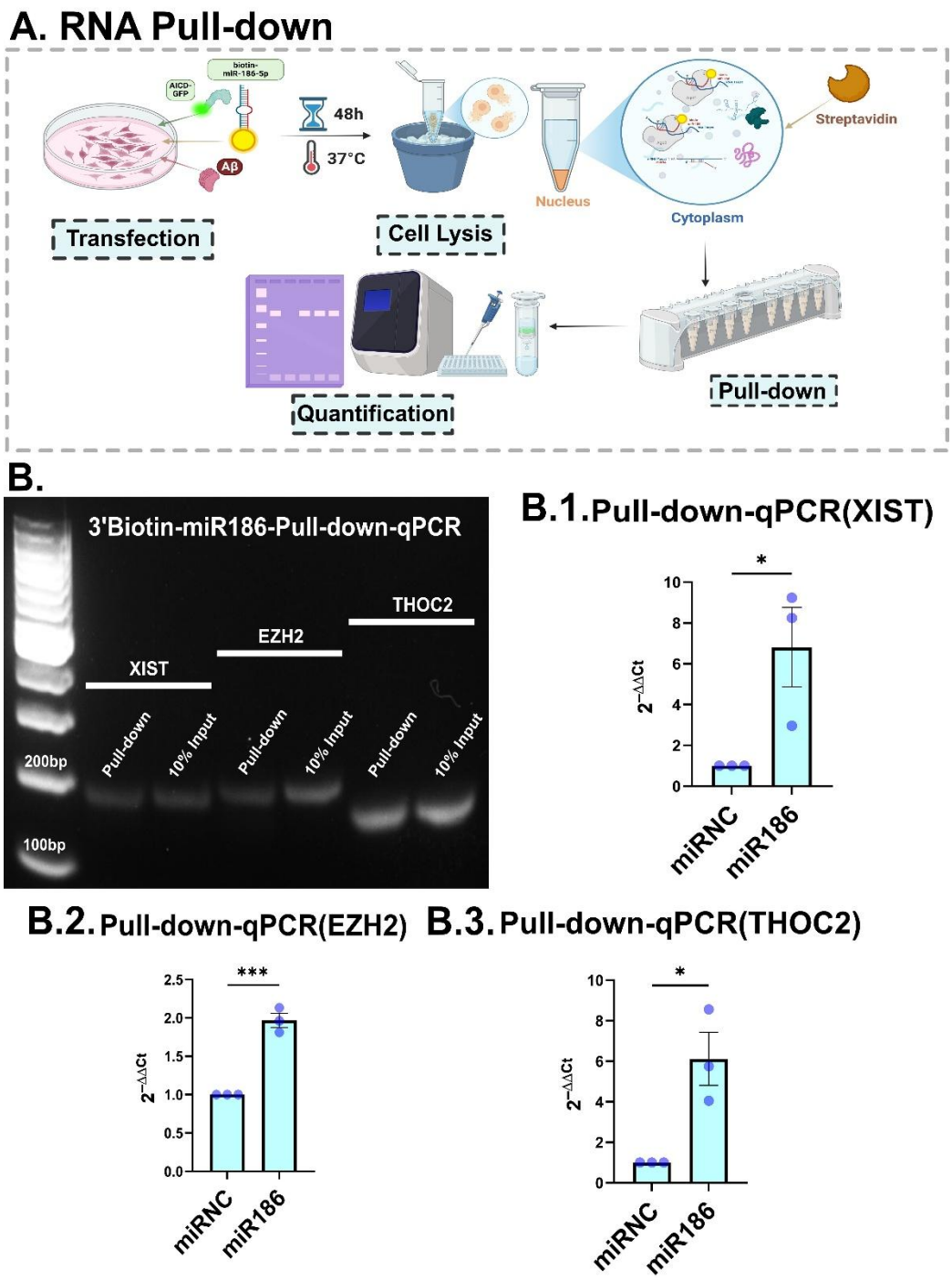

Figure 9. Cytoplasmic interaction of miR-186 with XIST, EZH2, and THOC2 confirmed by biotinylated RNA pull-down assay. (A) The 3'biotinylated miR-186 mimic was transfected in the AD cell model and pulled down using streptavidin coated magnetic beads. The pulled-down RNA was then detected and quantified using qRT-PCR. (B) Representative agarose gel image showing successful pull-down of XIST, EZH2, and THOC2 transcripts from the cytoplasmic fraction of AICD+Aβ(AD)-treated cells using a 3'-biotin-labeled miR-186

963 ***mimic. A 10% input RNA was used as a loading reference. (B.1–B.3) qRT-PCR***
964 ***quantification of pull-down products revealed significant enrichment of XIST (*p < 0.05),***
965 ***EZH2 (***p < 0.001), and THOC2 (*p < 0.05) transcripts in the miR-186 pull-down fraction***
966 ***compared to the miR-NC control, confirming RNA-RNA interactions. Data were normalized***
967 ***with 2% input samples and represent mean ± SEM from biological replicates. Statistical***
968 ***significance was determined using unpaired student's t test.***

969

970

971

972

973

974

975

976

977

978

979

980

981

982

983

984

985

986

987

988

989 **Supplementary Figures**

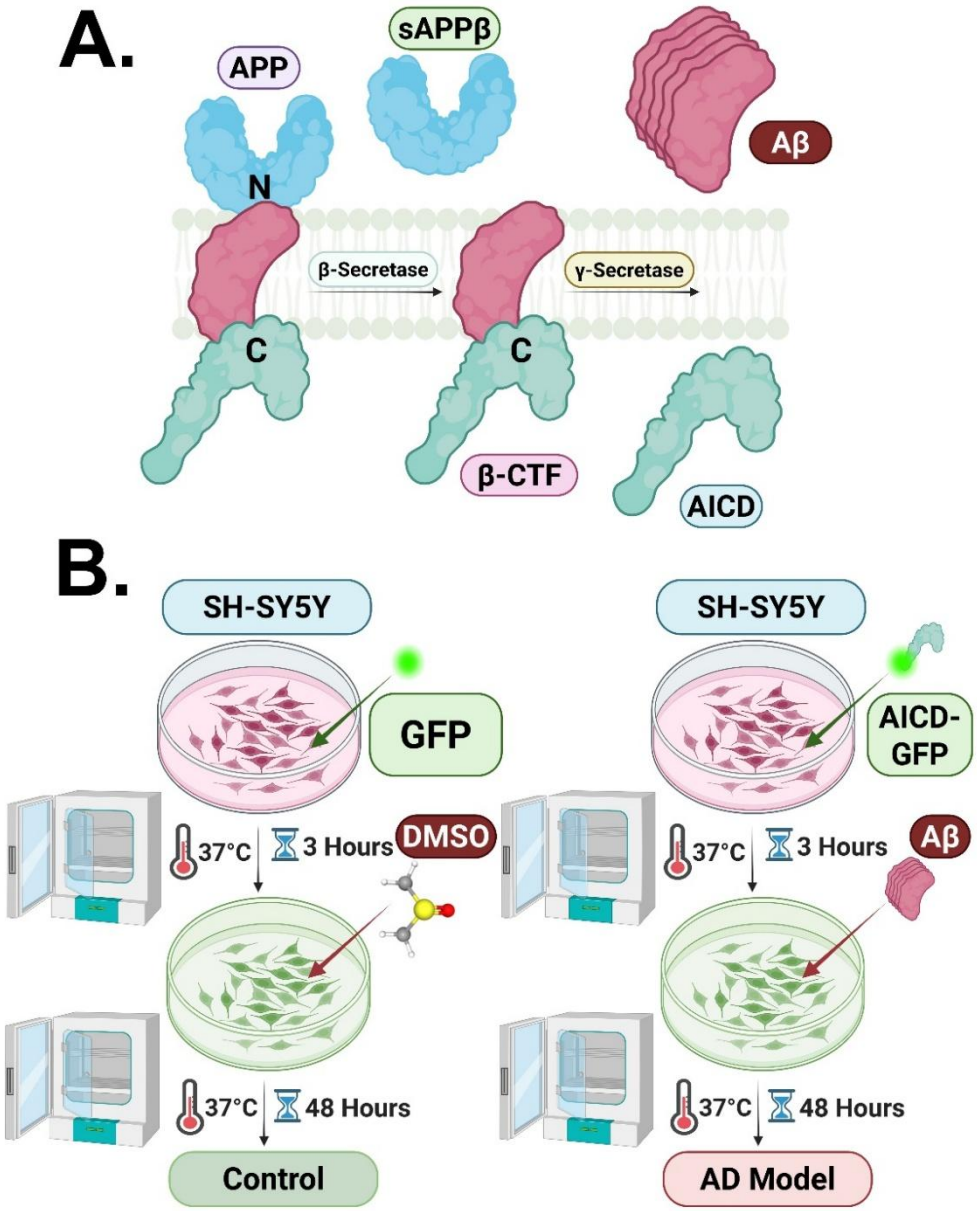

990

991 ***Figure S1. (A) In the amyloidogenic processing of APP, sequential cleavage by β-secretase***
992 ***and γ-secretase produces soluble APPβ (sAPPβ), the APP intracellular domain (AICD), and***
993 ***amyloid-β (Aβ) peptides. Aβ aggregates outside the cell, while AICD moves to the nucleus,***
994 ***where both fragments contribute to AD-related cellular pathology. (B) Schematic of the in***
995 ***vitro AD cell model. SH-SY5Y cells were transfected with either GFP (control) or AICD-GFP***
996 ***(AD model). After 3 hours, control cells were treated with DMSO, whereas AD cells were***
997 ***given Aβ peptide to mimic amyloidogenic stress. The combined presence of AICD and Aβ***

recapitulates the dual pathogenic signaling axis, and cells were kept at 37 °C for 48 hours before further analysis.

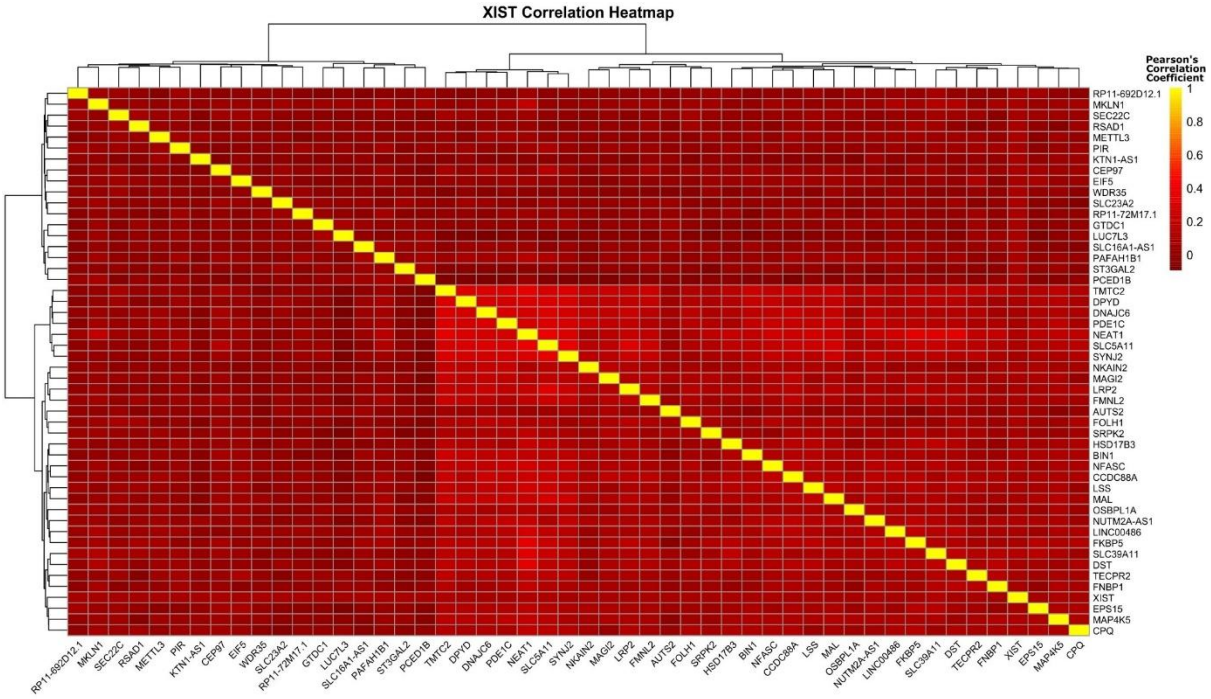

Figure S2. The heatmap shows the top 50 genes positively correlated with XIST in female neurons.

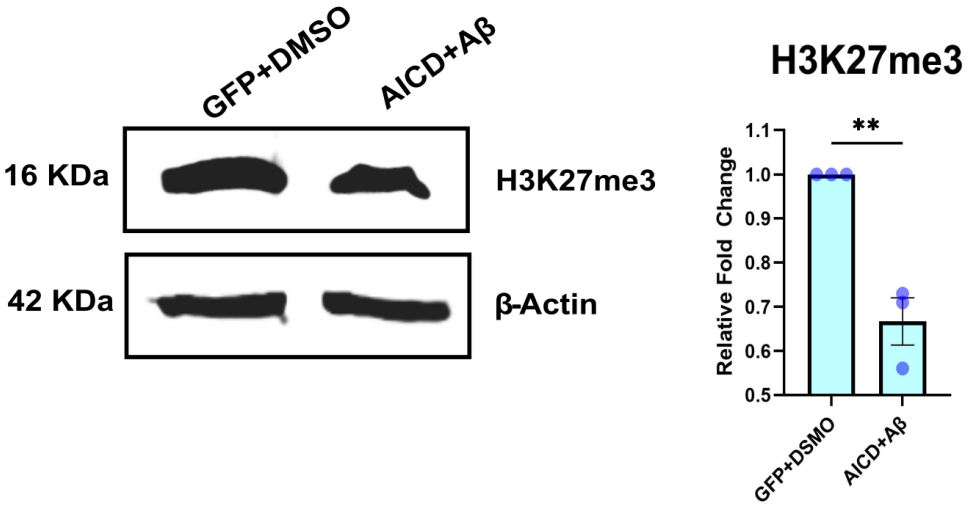

Figure S3. The global H3K27me3 levels were measured using western blots and was found to be significantly downregulated in AD (AICD+Aβ) compared to control (GFP+DMSO). Error bars represent mean ± SEM; significance was determined using an unpaired Student's t test.

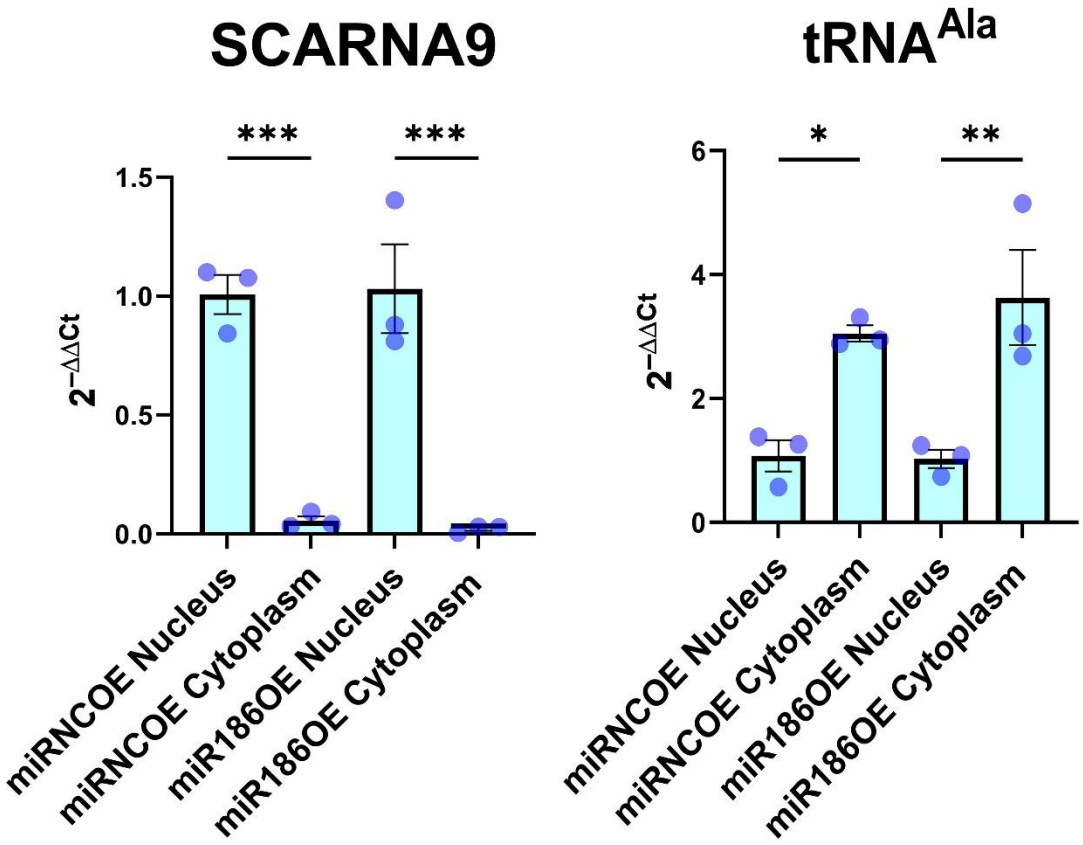

Figure S4. Validation of fractionation efficiency in biotinylated RNA pull-down. (A) SCARNA9 was significantly upregulated in the nucleus compared to the cytoplasm. (B) tRNA-Ala was significantly upregulated in the cytoplasm compared to the nucleus. Error bars indicate mean ± SEM; statistical significance was determined using one way ANOVA followed by Bonferroni post hoc test.

1023 **Supplementary Table**

1024 **Table S1. The list of primers for qPCR**

S. No.	genes	Primer Sequences
1	XIST	FP: CACCCCACCCTTAGTTTCCC
		RP: CACACAAGGGGCAGAGAGAG
2	EZH2	FP: GAGTTGGTGAATGCCCTTGG
		RP: TGCTGTGCCCTTATCTGGAA
3	THOC2	FP: TCACTTCTTCCAGCCAACCA
		RP: CGCCGAACATCAGGACTTTC
4	SCARNA9	FP: GATCTCTACAGTTCTGAGAAGCA
		RP: TGCCCAGAAATGATTAGGCTT
5	miR-186-5p	Stem loop: GTCGTATCCAGTGCAGGGTCCGAGGTATTCGCACTGGATACGACAGCCCA
		FP: AAGCGCCTCAAAGAATTCTCC
6	18S rRNA	FP: GGCCCTGTAATTGGAATGAGTC
		RP: CCAAGATCCAACTACGAGCTT
7	β-actin	FP: CACCATTGGCAATGAGCGGTTC
		RP: AGGTCTTTGCGGATGTCCACGT
8	tRNA-Ala	FP: AGCTCAGTGGTAGAGCGCA
		RP: GGGGATCGAACCGAGGC
9	THOC2-promoter	FP: CGGGAGCTGAGAGTTCGTTT
		RP: GGGAAGTAAGGCCGAAGACT

1025